Approved for public release;
Distribution unlimited

NAVENVPREDRSCHFAC
Technical Paper No. 18-75

(12) B.S.

ISLAND BARRIER EFFECTS ON SEA STATE AND ATMOSPHERIC MOISTURE AS DETECTED BY A NUMERICAL WAVE MODEL AND SENSORS OF THE DEFENSE METEOROLOGICAL SATELLITE PROGAM (DMSP)

by

ROBERT W. FETT
and
KEVIN RABE

OCTOBER 1975

NAVAL ENVIRONMENTAL PREDICTION RESEARCH FACILITY
MONTEREY, CALIFORNIA 93940

UNCLASSIFIED

SECURITY CLASSIFICATION OF THIS PAGE (When Data Entered)

REPORT DOCUMENTATION PAGE

READ INSTRUCTIONS BEFORE COMPLETING FORM

1 REPORT NUMBER: NAVENVPREDRSCHFAC Technical Paper No. 18-75

2. GOVT ACCESSION NO.

3. RECIPIENT'S CATALOG NUMBER

4. TITLE (and Subtitle): Island Barrier Effects on Sea State and Atmospheric Moisture as Detected by a Numerical Wave Model and Sensors of the Defense Meteorological Satellite Program (DMSP)

5. TYPE OF REPORT & PERIOD COVERED

6. PERFORMING ORG. REPORT NUMBER

7. AUTHOR(s): Robert W. Fett and Kevin Rabe

8. CONTRACT OR GRANT NUMBER(s): WF52-551

9. PERFORMING ORGANIZATION NAME AND ADDRESS: Naval Environmental Prediction Research Facility, Monterey, CA 93940

10. PROGRAM ELEMENT, PROJECT, TASK AREA & WORK UNIT NUMBERS: PE: 62759N PN: 52551; TA: WF52-551-713; NEPRF WU: 054.2-4

11. CONTROLLING OFFICE NAME AND ADDRESS: Naval Air Systems Command, Department of the Navy, Washington, D.C., 20361

12. REPORT DATE: Oct 1975

13. NUMBER OF PAGES: 67

14. MONITORING AGENCY NAME & ADDRESS (if different from Controlling Office): 71p.

15. SECURITY CLASS. (of this report): UNCLASSIFIED

15a. DECLASSIFICATION/DOWNGRADING SCHEDULE

16. DISTRIBUTION STATEMENT (of this Report)

Approved for public release; Distribution Unlimited.

17. DISTRIBUTION STATEMENT (of the abstract entered in Block 20, if different from Report)

NEPRF-Technical Paper-18-25

18. SUPPLEMENTARY NOTES

19. KEY WORDS (Continue on reverse side if necessary and identify by block number)

Island Barrier Effects
Ocean Waves and Swell
Meteorological Satellites
Numerical Modelling
Eddies
Bow Wave Effect
Atmospheric Moisture
Sea State

20. ABSTRACT (Continue on reverse side if necessary and identify by block number)

Island barrier effects on sea state and atmospheric moisture have been studied through use of a numerical wave model and examination of data from the Defense Meteorological Satellite Program (DMSP). It is found that calm areas do not extend an appreciable distance downstream. However, swell refraction effects cause a reduction in swell height, a change in swell period, and a reorientation of swell

Next page

DD FORM 1 JAN 73 1473 EDITION OF 1 NOV 65 IS OBSOLETE S/N 0102-014-6601

UNCLASSIFIED

SECURITY CLASSIFICATION OF THIS PAGE (When Data Entered)

407 279

20. Abstract (continued)

direction, long distances to the island's lee, which may account for the satellite-observed reflective patterns noted in sunglint situations over those areas. 'Bow-wave' effects appear to be similarly observed due to sunglint from reoriented swell patterns.

In conditions of a strong low-level inversion, DMSP data, being sensitive to water vapor absorption, reveal dry plumes extending downwind from islands. These dry plumes are apparently caused by the island's drying effect on atmospheric flow as it passes over and is influenced by topographical features of the island barrier.

CONTENTS

1. INTRODUCTION 3

2. GEOMETRICAL ASPECTS OF DMSP SUNGLINT RELATIONSHIPS 5

3. ISLAND BARRIER EFFECTS AND SEA STATE INFLUENCE 7

4. THE FRENCH SPECTRO-ANGULAR WAVE MODEL 11

   a. Island Barrier Effects on the Height of Swell in the Lee of Islands 13

   b. Swell Directional Changes in the Lee of Islands -- Eddy Formation 13

   c. Swell Periodicity Changes in the Lee of Islands 14

   d. The Bow-Wave Effect 15

5. SOME DMSP EXAMPLES OF ISLAND LEE EFFECTS 16

6. ISLAND "BOW WAVE" EFFECTS REVEALED BY DMSP 18

7. AIRFLOW RELATIONSHIPS TO ISLAND TOPOGRAPHY 20

8. ISLAND BARRIER EFFECTS ON ATMOSPHERIC MOISTURE . . 26

9. CONCLUSIONS 32

REFERENCES 33

APPENDIX A -- MATHEMATICAL FORMULATION OF THE FRENCH SPECTRO-ANGULAR WAVE MODEL, DSA V 37

FIGURES 43

1. INTRODUCTION

Swell refraction around island barriers is a well known phenomenon. The effect can be quite pronounced depending on local bathymetry. Wilson et al. (1973) described swell refraction around the island of Aruba, off the coast of Venezuela, where swell was observed traveling from the west, against the prevailing trade wind flow, to strike a beach on the lee of the island, after having been refracted over 90° from the island's northwestern tip. Other studies (Strong et al., 1974) have suggested that islands exert a blocking effect on atmospheric flow and oceanic swell, resulting in relatively calm winds and calm seas which extend long distances to the lee of the islands. Effects in sunglint areas where solar reflection can be influenced by the relative calmness of the surface of the sea are thought to result from such blocking and have been detected by satellites.

The wave refraction concept and the island blocking concept are not necessarily at odds with one another since absolutely calm wind and sea conditions have certainly been observed in the lee of islands. On the other hand, questions of magnitude of effect, under wind flow of a given strength, arise which suggest the desirability of a more quantitative approach.

In the study reported here a numerical wave model was applied to the task of predicting the height, period and direction of swell around an island under the assumption of uniform wind fields, except for the lee of the island where a blocking effect is assumed and wind speeds are significantly reduced.

The study also re-examined typical reflective patterns detected by satellite in the lee of islands, under conditions

of sunglint; the possibility of bow waves created by water currents flowing past an island; and, in general, the nature of the sunglint problem around island barriers. Emphasis was given those data received by polar orbitting satellites which employ scanning radiometer type sensors. In particular, the characteristics of the Defense Meteorological Satellite Program's (DMSP) sensors were examined. Data from such sensors are unique in that an expanded spectral interval was sampled, which extends into the near infrared (IR) wavelengths, where water vapor absorption by the atmosphere reduces transmittance in areas of heavy water vapor concentration.

The possibility that island barriers, under conditions of strong low level inversions, exert a profound drying influence on air flowing to the lee has been predicted by numerical, mesoscale models (Lavoie, 1974). The DMSP sensor sensitivity to water vapor concentrations suggests that this effect should be detectable. Typical DMSP samples related to this question are analyzed in a discussion of island barrier effects on atmospheric moisture.

2. GEOMETRICAL ASPECTS OF DMSP SUNGLINT RELATIONSHIPS

Sunglint patterns are apparent in most of the daytime DMSP passes. The effect will be minimized for a direct readout site in the N. Hemisphere at the winter solstice and maximized as the sun progresses to a summer solstice position, depending on the northern latitude of the direct readout location. An example of a typical sunglint pattern obtained in a direct readout at San Diego, California is shown in Figure 1. The sunglint pattern stretches from bottom to top in the central portion of the figure. In this example the sub-satellite track (dashed line) passes just to the left of the major axis which would separate the sunglint pattern into two nearly symmetrical halves. General aspects of the pattern can be explained by referral to the schematic of Figure 2.

As the spacecraft progresses northward at an altitude of 450 n mi(833 km), from point A to point D, points of possible specular reflection (where zero or horizontal slope reflection occurs) are located along great circle arcs, connecting the subsatellite point with the subsolar point. The approximate distance to any point X can be calculated by applying the nomogram in Figure 3. However, the satellite is capable of detecting specular reflection only at point B, since the scanning radiometer sweeps from horizon to horizon perpendicular to the subsatellite track. Sunglint detected at other points such as A and C is non-specular, and possible only because of diffuse reflection off a disturbed sea, with wave fronts appropriately oriented to provide the required geometry. Sunglint continues to be detected with steadily decreasing intensity beyond point C until arrival near point D, where

the scanner is no longer capable of viewing any portion of the sunglint area. Maximum reflectivity is normally sensed along the curve connecting all points of possible specular reflection. This accounts for the pattern shown in Figure 1, including the displacement of the band from the subsatellite track. Sea state and atmospheric conditions can act to modify this pattern such that sunglint effects may not be detected or, if detected, appear asymetrical or offset from the anticipated pattern.

Figure 4 is a DMSP pass over the western Pacific in which brilliant specular reflection is observed near 30° North latitude. This brilliant specular reflection is the result of a relatively calm sea state. The anomalous dark areas to either side are also interpreted to be calm, as discussed by Parmenter (1969) and McClain and Strong (1969).

Figure 5 gives a theoretical sea surface sunglint composite pattern which relates to this example. The dark swath represents calm conditions in an otherwise uniform wind field of 5m sec^{-1}. A reflectance measurement of 5000 units is indicated at the specular point. Reflectance is reduced drastically east and west of this point in the calm area, resulting in the very dark shades, as shown in the actual example of Figure 4. An important implication is that, away from the immediate vicinity of the specular point, calm sea states should appear much darker than the surrounding non-calm seas. It is this relationship which, in the following sections, will be applied to interpretations of observed reflectance patterns.

3. ISLAND BARRIER EFFECTS AND SEA STATE INFLUENCE

Wind variation over the waters surrounding islands under steady trade wind flow have been noted to vary quite dramatically as a result of island topography. For example, Patzert (1969) in a Hawaiian Island study, found a distinct wind minimum in the lee of each island while stronger winds consistently blow in the channels between islands in a manner analogous to Venturi flow through constricted openings.

Visual evidence supporting Patzert's study was obtained by astronauts participating in the flight of Gemini IX on 6 June 1966 as they photographed the Canary Island area (NASA, 1968). They noted a distinct dark area extending a short distance to the lee of several of the islands which were otherwise sharply illuminated by sunglint reflecting into the camera system. They attributed the effect to the sheltering influence of the islands which apparently produced a calm area to the lee. The calm area reflected all light away from the camera instead of scattering it through wave action as did the adjacent areas. Stevenson (1970a), in a review of Apollo 9 photographs of the Cape Verde Islands on 9 March 1969, noted similar areas revealed in sunglint. It was his contention, however, that the effect was a turbulent feature or wake resulting through wave refraction around the island and that the wake was but one of a series which formed and then shed off from the island. He contended that the series extended in a broken pattern at least 222 km downstream from the island group (Stevenson, 1970b).

Cram and Hanson (1974) studied ERTS-1 (Earth Resources Technology Satellite) data over the Antilles Islands in an

attempt to relate distinct features noted on the lee of each island to ocean eddy formations, as suggested by Stevenson. They were unsuccessful in this attempt and concluded that the features observed resulted from horizontal differences in sea surface roughness, due to the wind-shadow effect of the islands. Essentially, they felt that the influence of island topography on air flow was the main cause of the ocean features observed. Cram and Hanson's conclusions were similar to those of an earlier study by Strong, et al. (1974) over the same area.

Strong concluded that the reflectance patterns observed by means of NOAA-2 (Figure 6) were due to differences in surface roughness between the open sea and the sheltered zone directly in the lee of the islands. The reflective patterns, then, were assumed to be calm or relatively calm seas (heights less than 1/2 m) in comparison to seas of the surrounding area (heights about 1 m). In the broader perspective of NOAA-2 as opposed to ERTS, they found that these patterns extended about 200 km downwind under wind speed conditions of about 5 m sec^{-1}.

If the geometrical reasoning developed in the early part of this paper is followed, it appears that an alternate explanation for these patterns may more accurately account for these features as observed by NOAA-2. A calculation of specular point location for the data on 29 September reveals it to be over 300 km west of Guadeloupe at the time the spacecraft was viewing that area. The main zone of specular reflection is well to the southwest of the islands, as can be seen near the bottom of the depiction. The islands, therefore, are on the very fringe of the diffuse sunglint area. Accordingly, calm areas or relatively calm areas should appear darker than the surrounding seas and not lighter.

In fact, Strong (1974) noted small dark areas in the immediate lee of the islands, on September 29, 1973 (Figure 6). By the reasoning presented here, these features should correlate with extremely calm seas. The reflective patterns extending beyond the small dark areas cannot, however, represent calm seas, but, more reasonably, result from greater concentrations of diffuse reflection, brought about by a reorientation and change in characteristics of the wave fronts in the lee of the islands.

Figure 7 is a schematic which shows how refractive patterns around an island can lead to local variations in sea state resulting in a "shadow of turbulence" in the lee of the island which could explain the noted change in reflectivity. Wind variations, one might anticipate, could rapidly disrupt this pattern and exert an over-riding influence on sea state, depending on the strength of flow. Cram and Hanson (1974), for example, found that winds of 5-8 m sec^{-1} produced well defined features, while speeds near 10 m sec^{-1} caused a noticeable reduction in the size and sharpness of features observed.

The NOAA-2 view of 3 October 1973 (Figure 6) is interesting in this respect since the island of Marie Galante (small, dark, area just south of the arrow pointing to Guadeloupe Island) exhibits no reflective lee effect. Since the highest point on this island is only 205 m, its ability to restrict airflow to the lee is limited. The refractive wave pattern around the island, therefore, is apparently over-ridden by the force of the wind so that wave forms in the lee of the island are similar to those in the surrounding area. Valley areas on the main islands similarly allow the passage of winds which immediately disrupt the lee refractive patterns so that alternate dark swaths are seen within the reflective areas.

If this interpretation is correct it must also follow that the reflective areas are areas of reduced wind speed. Thus winds may be relatively calm or lighter in these areas than in the outlying areas; on the other hand, the sea state cannot be calm but could be reduced (or heightened) due to the wave restructuring effect of refractive interference patterns.

4. THE FRENCH SPECTRO-ANGULAR WAVE MODEL

It is obviously desirable to document more fully typical effects of waves and swell under varying wind conditions with the flow interrupted by an island barrier. Unfortunately, an adequate sample of observations of this type is lacking. Numerical models based on certain simplifying assumptions, however, have been developed which have been successful in simulating a number of effects. One of the most successful of these has been the French Spectroangular Wave Model. This model, known as D.S.A. V (Densities Spectro-Angulaires V) was first developed by Gelci, Chavy and Devillaz (1963). The main advantage of this model is that it computes the sea state at each grid point from an energy spectrum of 16 directions and 6 periods, thus not restricting the energy growth to a singular component and allowing the spread of energy.

The model has been substantially verified for many purposes by comparison to wave observation and also wave recorders (Fons, 1966). The comparisons were consistently favorable and the model has since been utilized for a variety of research tasks, both in France and at the Environmental Prediction Research Facility (EPRF).

For this study the D.S.A. V was chosen over the various singular wave models available because its spectro-angular density approach accounts for angular advection and dispersion. Also, its spatial growth and decay features were vital in reproducing the effects produced by the interactions of the wave trains refracting around the island, and for the island's blocking effect on atmospheric flow which reduced wind speeds to the lee.

Mathematically, the basic method used by this model can be symbolized by the following equation:

$$\frac{de}{dt} = F\,[W,\ |\theta - w|,\ T] - \frac{Ae}{T^4}\, m_o - V_{(T,\theta)}\ \text{Grad}\ e_{(T,\theta)}$$

where the change in spectral density, $\frac{de}{dt}$, is described by a spectral increase term, a decay term and an advective term, dependent upon the group velocity. (See Appendix A for a detailed mathematical formulation.) It utilized the wind fields as its only driving force, assuming wave growth can be simulated by a single velocity, based on the wind velocity, W, wave period, T, and wind azimuth, /θ-w/ where w = wind direction, θ = computational direction. Decay is accounted for by the interaction of the sea state compenents, m_o, with each other and empirical attenuation coefficient of the wave trains, A. The advection term [$V_{(T,\theta)}$ Grad $e_{(T,\theta)}$] is a function of the gradient of the spectral density and the unit speed of the swell packet. $V = \frac{gt}{4\pi}$ where g is the acceleration of gravity.

A uniform wind field was assumed to exist at each grid point except in the lee of the island where, for 9 grid points extending 3 grid intervals (222 km) downstream, wind speeds were uniformly reduced to 2-1/2 m sec^{-1}. Island topographical blocking effects on atmospheric flow are, therefore, incorporated in the model presentation.

For the numerical results to be presented (Figures 8-16), a mesh length of 74 km (40 n mi) was utilized. The winds were introduced as a steady flow from the west and computations were made for 40 hours. A rotation has been applied to the output for ease of viewing, with a westerly wind flowing past the island from the top of the numerical output depictions to the bottom. Several trial velocities were separately used and the island was introduced as a square having sides of 148

km. It should be noted that the wave height fields reproduced are fields of H 1/10, the average height of the tenth highest wave, and not $\overline{H}$, the average wave height, which is approximately one-half the H 1/10 values.

a. Island Barrier Effects on the Height of Swell in the Lee of Islands.

The significant wave height calculations show a distinct shadow zone of reduced wave height in the lee of the island. Examples are shown in Figures 8, 9, and 10, for the 7-1/2 m sec^{-1}, 10 m sec^{-1}, and 15 m sec^{-1} wind speed conditions. Several features are readily apparent. Of greatest interest is the indication that relatively calm conditions extend for only about 1 grid interval (74 km) downstream from the center of the island, regardless of the background wave height and wind speed. The area of most reduced heights, similarly, extends downwind in a narrow cone, several more grid intervals from the center of the island. The indications of calm seas, immediately adjacent to the island, correspond almost perfectly with the positions of the small, black areas in the lee of the Lesser Antilles on 20 September 1973 (Figure 6). (See also similar areas in Figure 30.) Sea heights increase rapidly in all directions around the relatively calm areas but are reduced in value by as much as about 40% in comparison to sea heights in the unprotected areas.

b. Swell Directional Changes in the Lee of Islands - Eddy Formation.

Directional changes corresponding to the sea height changes are shown in Figure 11 for the case of a uniform wind speed of 7-1/2 m sec^{-1}. A turbulent lee eddy effect is

is apparent in this example. Similar eddies have been directly observed by Barkely (1972), Patzert (1969), White (1973) and others.

Eddies are commonly associated with the mass transport and velocity fields and it should be noted that this model does not directly compute these fields. What results is an implied velocity field based on the distribution of wave energy throughout the spectrum at a given point. A resulting shift in the direction and period at maximum energy can, therefore, be construed as directly implying a corresponding shift in the wind-induced current flow and direction.

Eddies are commonly found along oceanic fronts, along continental shelves, and in the lee of islands. Due to the 74 km grid interval, many eddy effects are undoubtedly masked (in terms of defining precise directional changes). However, some additional eddy effects seem to be revealed through anomalous changes in periodicity, 5 grid intervals downstream from the island, as shown in Figure 12.

c. Swell Periodicity Changes in the Lee of Islands.

An example of the swell periodicity is shown in Figure 13. Longer period swell directly in the lee of the island contrasts with shorter period swell in adjacent areas and further downstream.

The combined effect of reduced swell height, with shorter periods and changed direction downstream (including turbulent eddy effects) as predicted by the numerical model, appear to justify the nomenclature "shadow of turbulence" referred to in the discussion of Figure 7. Again, it is this changed sea state configuration rather than "calm" or "relatively calm" seas which appears most likely to explain the satellite-

observed reflective patterns extending long distances in the lee of islands under conditions of sunglint.

d. The Bow-Wave Effect.

The numerical output showed effects, not only on sea state to the island's lee but also along the edge and to the rear of the islands, spreading out in a manner similar to that of the bow wave made by a ship passing through the water. The effect was most pronounced in the wave height depictions as typified by the example in Figure 14. The corresponding directional field is shown in Figure 15. The change in direction to 247° on the south side of the island, and 292° on the north side of the island, suggests a bow wave effect.

Again, the large grid size necessitated by the model prevented detailed inspection of this feature, and the possibility remains that this is an area of pronounced swell refraction as noted in Figure 7. An entire spectral breakdown of all component energy was made for both points of anomalous direction, and is shown for the point on the southern side of the island in Figure 16. A distinct shift in the energy spectrum from the east to the east-south-east is apparent, indicating a definite bending of the swell fronts at these points. Again this could be either refraction or the bow wave effect. This possibility will be explored more fully in a discussion of DMSP data in a later section.

5. SOME DMSP EXAMPLES OF ISLAND LEE EFFECTS

Figure 17 shows an example of reflective lee effects in the wake of the Hawaiian Islands as viewed by the visual Very High Resolution (VHR) scanner of a DMSP satellite. At the time these data were recorded the subsolar point was located at 13.2 degrees North latitude and 108.3 degrees West longitude. The Hawaiian chain lies considerably northwest of this location with the specular point indicated by the "x", west of Hilo, Hawaii. The fact that brilliant reflection is not in evidence near this point can most reasonably be attributed to rougher seas in that area. This is the reverse of the more customary interpretation of sunglint patterns near the specular point, when the seas are calm, but is equally valid. As an example; Strong et al. (1972) documented a dark streak through brilliant reflection in the Gulf of Tehuantepec, and attributed it to a brisk northeasterly wind diffusing the specular reflection in that area. Note that the plotted wind reports show a rapid acceleration, from 7.5 m sec^{-1} to 15 m sec^{-1}, over the specular area, which would support a rapid increase in sea height. The ship report in the reflective pattern west of Oahu is especially important since a sea height of .9 m was indicated. This observation is consistent with the numerical wave height predictions and is additional verification that the reflective patterns, in general, are not calm as previously thought except in the immediate lee, but can actually represent a quite well developed sea state, though reduced in comparison to outlying areas.

Figure 18 is a view of the Hawaiian Islands on 30 June 1974. At the time the spacecraft was scanning the area of Oahu,

Hawaii, the specular point was almost 5 degrees of latitude to the east southeast. The Hawaiian Islands are on the very fringe of the sunglint area but lee effects cause an apparent sunglint wake. Again, the wakes cannot be calm or even relatively calmer than surrounding areas or they would appear darker. This pass also yields an important clue tending to suggest that island lee effects, as revealed by the DMSP sensor, may not be entirely oceanographic and that at times atmospheric effects may also be involved. Note that the grey shade defining an apparent wake effect west of Oahu, Hawaii continues inland over the southern portion of the island. Some attention is devoted to this aspect in a later section which discusses atmospheric effects.

6. ISLAND "BOW WAVE" EFFECTS REVEALED BY DMSP

A current flowing past a stationary obstacle in the water characteristically forms a bow wave similar to that produced by a ship moving rapidly through the water. It appears possible that an ocean current moving past an island might produce a similar effect. Emery and Stevenson (1972) discussed this possibility with respect to the island of Taiwan.

A Gemini X photograph of Taiwan revealed a standing wave at the south end of the island, possibly caused by the northward flowing Kurushio current which attains speeds as great as 3 km/hour. An alternate explanation offered by the authors for the existence of this feature was "...shallow internal (subsurface) waves rather than gravity waves." DMSP data shown in Figure 19 reveal a possible bow wave effect off the island of Socorra.

Surface observations (6 November, 0000 GMT) at Socorra indicated clear skies with surface winds from 010° at 8 m sec^{-1}. A ship just north of the island at 21.2 N, 111.1 W also reported clear skies with northerly winds and 1.35 m swell coming from 360°. The grey areas extending left and right of Socorra, and apparently drifting to the south, resemble bow waves which appear to be scaled to a size commensurate with an island the size of Socorra. With clear skies existing for hundreds of miles upwind from the island, it is difficult to conceive of any convergence effect that would give rise to barely resolvable cloudiness resulting in the grey snade extending from the island in such a fashion. The pattern is also quite different from cloudiness patterns normally observed adjacent to and in the lee of islands. The effect could be explained, however, as being due to diffuse sunglint from

ocean wave fronts re-oriented as a result of the island's barrier effect to the current flow. The specular point was about 3.82 degrees (424 km) south southwest of the satellite at the time it was scanning the Socorra Island area. It was, therefore, on the outer fringe area of where sunglint effects could be measured. Wave orientation in the outlying areas, away from Socorra, apparently does not favor transmission of diffuse sunglint into the spacecraft sensor. However, reorientation of wave direction, due to a bow effect, could result in such a transmission, and seems a most likely cause for the patterns observed.

An apparent bow wave effect has also been noted around other islands. Figure 20 shows a DMSP VHR sunglint depiction off the west coast of North America. Apparent bow wave effects can be seen off the islands of Cedros, San Clemente, San Nicholas, Santa Rosa and Santa Cruz. Note that in these instances the grey shades of the apparent bow wave have reversed tonality in comparison to the depiction of Figure 19. Such a reversal is the familiar one of satellite versus ray reflection angle geometry. If at some optimum location ray reflection into the spacecraft sensor is maximized, then at alternate locations for the same area it will be minimized, similar to specular point reflection effects off of a calm sea.

Figure 20 contains other island barrier effect examples which will be referred to in the discussion of atmospheric effects -- most notably the grey shade pattern surrounding Guadalupe Island and the crescent shaped cloud pattern upstream from Cedros Island.

7. AIRFLOW RELATIONSHIPS TO ISLAND TOPOGRAPHY

It is apparent that the satellite observed upstream and downstream effect of islands on sea state and atmospheric flow patterns vary greatly depending on a number of factors. These include not only sun angle relative to the satellite, but also island topography and bathymetry, speed and direction of atmospheric flow and ocean current flow, stability of the atmosphere, moisture content, presence or lack of an inversion, height of the inversion (if one is present), and changes in this height in the area surrounding the island. These factors can be combined in a large number of variations at any specific time.

Figure 21 illustrates in one picture the importance of topography in influencing downstream patterns. Shown are the islands of Socorro (lower left) and San Benedicto (upper right) located about 700 km south of the tip of the Baja Peninsula. Socorro has a 1200 m mountain which disturbs the flow sufficiently to produce an intricate pattern of mesoscale eddies. Previous studies have established that "...conditions necessary for development of these eddies are a strong low-level inversion which caps the stratocumulus field, an island barrier that pierces the inversion, and a persistent low-level wind flow in the 5-13 m sec^{-1} range" (Anderson, 1974).

This same study indicates that the eddies tend to break down if the wind speed exceeds 13 m sec^{-1} and that they will not form if the wind speeds are less than 5 m sec^{-1}. Isla San Benedicto does not have sufficient size or elevation to produce the eddy pattern but instead forms a long cloud trail to the south. A flow pattern which could explain the long

cloud trail is a helical or possibly circular circulation stimulated by the island causing upward vertical motion to the lee.

Island stimulation of upward vertical motion which continues downstream is attested to by thousands of satellite photographs showing cloud trails in the lee of islands all over the world. Figure 22 shows a typical example downstream from Guadalupe Island. Under conditions of northerly flow, Guadalupe frequently develops Karman type vortices to the lee, similar to those produced by Socorra, as shown in Figure 21. On this date, however, strong surface and upper level wind speeds did not permit the development of these cloud formations, but favored development of the long cloud trail visible to the south of the island. The 0000 GMT radiosonde observation (RAOB) for Guadalupe on 11 April 1974 reveals a low level inversion beginning near 700 m. Wave-like cloud formations superimposed on downstream cloudiness suggest a gravity wave inducement on the inversion caused by topographical features of the island which extend to a height of 1380 m. The alternate dissipation and generation of low level wave cloud forms emphasizes the sensitivity of the marine layer air to the effects of vertical motion in producing cloudiness.

Figure 23 shows the Guadalupe Island area on another day with flow from a different direction and a reduced speed (Northwest at 7-1/2 m sec^{-1}).

A lee effect is distinctly apparent, consisting of a black oval shaped area outlined by a uniform shade of grey which merges into stratocumulus type cloudiness. A downstream eddy is also apparent between Guadalupe and Cedros Island. Through arguments developed in preceding sections there is no reason to assume that the black oval-shaped area

consists of entirely calm seas as opposed to rougher surrounding seas and, through this mechanism, suggest that the features observed can be explained through effects of sunglint.

Additionally, this depiction is an enlargement taken from Figure 1. As can be seen from Figure 1, Guadalupe, at this time, was in an area where sunglint effects would not exist or would be very minimal due to the satellite scanning angle and sun geometry.

There is a suggestion that the grey shade outlining the black oval shaped area consists of a high concentration of haze droplets associated with the formation or dissipation of the stratocumulus cloudiness. Note that some of the cloud bands southwest of Guadalupe merge into the light grey shade area and, in fact, some of them cross the darker shade of grey, retaining row alignment as a light shade of grey rather than bright cloud.

If this hypothesis is correct, the black oval-shaped area could be explained as being dryer than the area covered by the lighter shade of grey. The haze area could be detected as a result of scattering of light from the haze droplets back toward the satellite sensor. For scattering to be effective, the ratio of the particle size to the wavelength of incoming radiation should be on the order of one tenth or less (Johnson, 1954).

At .75 μ the wavelength of peak response for the DMSP VHR sensor (See Figure 29), this implies condensation particle diameter sizes on the order of .08 μ. As discussed by Beyers (1944), such particle sizes imply relative humidities of about 80% and are commonly associated with areas of increasing haze that gradually merge into fog or stratus type cloud formations.

A comparison of DMSP data with ERTS data showing cloud dissipation off the west coast of the United States confirms the tendency of the DMSP VHR sensor to display areas of cloud dissipation (or formation) as a uniform shade of grey. Figure 24 shows a DMSP, VHR, depiction at 1613 GMT on 22 May 1974. The main area of interest is the boxed, coastal area extending from San Luis Obispo Bay, past the Vandenberg Air Force Base area to Point Arguello, California. Cloud form appearance suggests fog or stratus over the water area. Note that the edge of the stratus has already changed from a visible bright cloud appearance to a uniform "anomalous" shade of grey.

Less than two hours later, at 1806 GMT, the ERTS satellite view shown in Figure 25 was obtained over the same area. As can be seen, the stratiform cloudiness has largely dissipated except for a small portion over San Luis Obispo Bay. Remaining cloudiness appears to be a thin deck of stratocumulus. Approximately 45 minutes later, at 1850 GMT, a second DMSP pass by another spacecraft viewed the same area (Figure 26). Cloud dissipation at this time is apparently almost complete. The remaining stratus over San Luis Obispo Bay, for example, is not detected as a bright cloud area but only as a shade of grey. The other stratocumulus cloud area also has apparently dissipated but similarly is still revealed as a uniform shade of grey. A close examination of this figure also reveals a narrow, light grey shade extending northward along the California coastline from San Luis Obispo Bay. Very misty or hazy, high humidity conditions are often noted in this narrow coastline strip created as a result of the release of condensation particles ejected into the air from the action of breaking surf.

The sequence, then, clearly suggests that the light grey shade areas often revealed by the DMSP VHR sensor at the edge of stratus or stratocumulus cloud areas and along coastlines, are areas of heavy concentration of condensation particles or haze droplets. Low level visibilities in these areas should correspondingly be reduced. Adjacent dark areas, similarly, do not exhibit this reflective quality and should therefore consist of much dryer air with increased low level visibility.

Referring back to the Guadalupe Island example (Figure 23), the conclusion can be drawn that dryer, clearer air exists downstream from Guadalupe over the black oval-shaped area. Carrying this argument one step further, it can be hypothesized that the island has exerted a downstream drying effect on air flowing over its surface.

In Figure 27, a DMSP VHR depiction, a consistent sequel to the Guadalupe Island example is demonstrated in the lee of the island of Socorra. A long cloud trail extends southward from San Benedicto, but Socorra, in addition to generating Karman type vortices well to the south, has apparently caused a drying influence downstream and created an elliptically shaped dark area in its lee. Note that the cloud trail of San Benedicto tends to dissipate over the dark area but appears to regenerate slightly further downstream. This same tendency is shown in Figure 21 where the cloud trail of San Benedicto dissipates over the dark area in the lee of Socorra but strengthens in intensity once it is beyond this apparent drying influence.

It is instructive to note the many meteorological interpretations that can be immediately and, very accurately, gleaned from this single DMSP depiction. First, the presence of Karman type vortices south-southwest of Socorra implies a strong low level inversion below 1400 m, the height of the

island. Hence, maximum low level cloud tops in the area should not exceed 1400 m. Low level wind direction can be deduced, from noting the lee effects, to be from the north-northeast at speeds of greater than 5 m sec^{-1} but less than 13 m sec^{-1} (speed requirements for the formation of Karman vortices). Areas of high low level humidity, and poor low level visibility, are implied by the light grey shades adjacent to the visible stratocumulus type cloudiness. Dark areas of increased low level visibility and lower moisture content can be presumed to exist over most of the eastern half of the depiction, and in a small area south of the island of Socorra.

8. ISLAND BARRIER EFFECTS ON ATMOSPHERIC MOISTURE

The Guadalupe and Socorra Island examples in Figures 23 and 27, as previously suggested, indicate a drying influence on the leeward air as it passes over and downstream from the island. Lee island dryness was the subject of a recent paper by Lavoie (1974). Using a single layer, mesoscale, numerical model, he studied aspects of trade wind weather on Oahu, Hawaii. He found that, because of the imposition of the mountain barriers in a trade wind inversion type situation, the low level relative humidity decreased significantly as the air passed over the islands. This was found to be in agreement with common observations including that of the greater comfort level normally attributed to the leeward coast. When the trade wind inversion was lowered in the model, the drying effect of the island was accentuated. Finally, when wind speeds were increased, with other conditions normal, extreme drying was noted downwind. He attributed the drying effect to a "rainout" of moisture on the windward side of the island; warming of the air as it passed over the island; and, most important, to a mixing of the marine layer air with dryer air across the inversion interface which lifted abruptly as the air flowed over and downstream from the island. He found that the greatest inversion heights occurred just off the leeward coast with an elevated inversion extending "...many tens of kilometers downwind of the island."

Environmental effects surrounding the island of Guadalupe (see Figure 20) add further support to the findings of Lavoie. First it can be seen from the plotted ship reports that north-northwesterly surface winds with speeds of 7-1/2 to 10 m sec^{-1}

could be anticipated in the Guadalupe area. The RAOB data (not shown) for Guadalupe at 1200 GMT, 21 May 1974, (approximately 4-1/2 hours prior to the DMSP data), indicate that an extremely pronounced inversion existed over the island at a height of about 250 m. The temperature at this level was +11°C with only a 1-1/2° temperature-dewpoint spread. At about 1500 m the temperature was +14°C and the dewpoint -16°C producing a 30° temperature-dewpoint spread in the extremely dry air above the inversion interface. Topographical features of the island itself extend well above the inversion in this dry air to heights of about 1380 m.

It is apparent that any induced upward vertical motion of the marine layer air, under these circumstances, would result in a pronounced drying tendency. It has been noted previously that the DMSP sensor appears to differentiate, in grey shade, dry air as opposed to air containing a heavy concentration of condensation particles.

However, another factor enters into the picture at this point. The DMSP spectral interval (.4 to 1.0 m) extends into the near IR where water vapor absorption becomes a significant factor. Figure 28 shows absorptivity curves for the entire atmosphere and for water vapor alone. It can be seen that there are several significant wavelengths where water vapor absorption in the near IR is pronounced. As an example, atmospheric transmittance is reduced to about 47% for one airmass thickness and to about 22% for two air mass thicknesses in the .94 micrometer absorption band. As a result of the double path length of solar radiation reaching the satellite, an increase in water vapor content will significantly reduce the amount of radiation reaching the sensor (AWS, 1974). At the same time the sensor's response at this wavelength and

other near IR wavelengths is very strong (Figure 29). The obvious conclusion is that a decrease in water vapor over an area should allow more light to be reflected resulting in a brighter area, assuming the satellite is in the proper position to receive this reflected light. (From an alternate position the area would appear darker.) Areas of heavy water vapor concentration should appear much darker regardless of the satellite's position. (Note, however, that a heavy concentration of condensation particles capped by an inversion with dry air aloft will be strongly reflective and appear as a light area).

Returning to Figure 20, and focussing attention on the Guadalupe Island area, one point of great significance is immediately apparent. There is an upstream-effect of the island which apparently influences the sensed reflectivity in that area. There is little reason to assume oceanographic influences. Water depths of over 1000 fathoms exist in the lighter area and swell should not reverse or reorient appreciably upstream from an island. However, 7-1/2 to 10 m sec^{-1} surface winds converging against the northern face of the island should result in upward vertical motion, resulting in an immediate drying tendency due to the pronounced inversion and dry air aloft. Heavier concentrations of water vapor in outlying areas would, because of atmospheric absorption characteristics, make these areas appear darker. Similarly, the downstream plume, which has a noticeable turbulent curl to it, is considered to be a dry atmospheric plume resulting through vertical motion and mixing with dry air downstream from the island. As discussed earlier, such vertical motion with a higher inversion frequently gives rise to long moist cloud trails (see Figure 22). Thus

upward vertical motion can produce opposite results, one dry, one moist, depending on the unique circumstances prevailing in each specific instance. There are several high level clouds in the area of Guadalupe southeast and southwest of the island. Note that each of these casts a distinct shadow in the proper direction as shown by the specular point-sun arrow relationship. However, as one might hope, the dry plume casts no shadow.

The crescent-shaped cloud upstream from Cedros Island also suggests upstream vertical motion, but in this case condensation is apparently reached and mixing minimized as the cloud spreads out laterally under the strong inversion. Referring again to another day (Figure 23) a crescent shaped clear area may be seen upstream from the island where vertical motion condition apparently caused immediate drying in an area with a shape similar to that of the crescent cloud.

All of these examples, of course, demonstrate the value of sunglint data in revealing direction of low level flow, as well as implications concerning the vertical structure and stability of the atmosphere.

A final, very dramatic example of atmospheric and oceanographic details revealed by the DMSP VHR sensor is shown in Figure 30. This example is in the area of Borneo and Celebes. A notable oval shaped plume extends northward over 5° of latitude from the northern peninsula of Celebes. The specular point is located within the area of the plume. The sun/satellite geometry is such that, had seas been relatively calm in this area, brilliant specular reflection would have been observed. Seas were not calm and, hence, only diffuse sunglint is received.

Southerly wind direction is easily inferred from the alignment of the plume and the observation that clouds have built up along the mountains on the southern coast of the peninsula. Mountain peaks on the peninsula extend to heights of about 2000 m. The black plume-like area adjacent to the light area along 123° east longitude is in the lee of a major valley in the Celebes Peninsula. It is unfortunate that RAOB data are not available to support the documentation of this particular example. However, based on previous discussion it seems reasonable to infer that the light plume-like feature is a dry plume over an essentially clear area resulting, as Lavoie suggested, from a rainout of moisture on the windward side of the peninsula, from additional heating of the air as it passed over the peninsula and, finally, assuming an inversion over the area, with a mixing of the marine layer air with dryer air aloft. The black plume-like feature in the lee of the valley is almost certainly, primarily, oceanographically caused. Wind flowing through the valley area between mountain ranges is funneled in Venturi fashion, giving rise to much stronger southerly flow than that in existence over the lighter oval-shaped area. The roughening of the sea surface diffuses the solar reflection so that little is deflected toward the spacecraft sensor. Additionally, the valley air is not lifted to any appreciable extent so that little mixing occurs and water vapor absorption becomes an important factor in reducing transmittance.

This dark plume has been detected repeatedly in DMSP data suggesting that this area is favored for strong winds and rough seas. Strong, et al. (1972) reported a similar feature over the Gulf of Tehuantepec (South-west coast of Mexico) in which a sunglint pattern was similarly disrupted.

The ability of the DMSP sensor to very markedly delineate such areas suggests applications in terms of detecting "Mistral", "Bora," and other dangerous wind events throughout the world, as they occur, in time for early warning and for use in short period coastal and oceanic forecasts.

The sun direction arrow in this example is pointing toward a small island within the broad oval-shaped light area. This island, Sangihe, exhibits lee effects similar to those discussed in the Guadalupe Island example (see Figure 23) with, however, shading reversed due to a changed satellite-sun geometry. In the Guadalupe example the scanning radiometer was sensing reflectivity in a direction away from the sun and the oval-shaped lee area appeared black, because the sun's rays were deflected away from the satellite. In the case of Sangihe, when the scanning radiometer passed over this area it was pointing toward the sun; hence, it measured increased reflectance producing a light grey shade depiction. In both instances a lee island-induced drying effect is inferred. Note that while Guadalupe produced a visible cloud eddy to its lee, Sangihe also produced a similarly shaped eddy which extends northward from the northern tip of the island as a darker grey shade of presumably moister air.

9. CONCLUSIONS

It has been the intent of this paper to more completely explore island barrier effects on sea state and atmospheric moisture through the incorporation of a numerical wave model and through the sensors of the DMSP system. The wave model clearly indicates that calm seas normally do not extend great distances to the lee of the islands although there is a reduction in swell height and changes in swell orientation. The change in swell orientation, along with reduced height and shortened period, is regarded as the major contributor to reflective patterns sensed by satellite when viewing islands in sunglint areas. A similar change in swell orientation apparently reveals the "bow wave" effect of an island on ocean currents moving past the island obstacle. Strong winds, induced by Venturi action, are revealed through a disruption of the sunglint pattern and effects of water vapor absorption. In conditions of a strong low-level inversion, DMSP data indicate a drying effect by the island, reducing humidities to the lee of mountains, producing dry plumes aligned with the low-level flow.

It is apparent that a great effort is required to adequately document through additional ground truth the effects that have been noted. The lengths and configurations of the dry plumes and lee reflective areas are related to several variables which may occur in many combinations. Future studies defining the unique combinations could be applied operationally in terms of understanding, semi-quantitatively, important aspects of atmospheric flow, thermodynamic structure, and sea state variability.

REFERENCES

Air Weather Service (AWS), 1974: Defense Meteorological Satellite Program (DMSP) User's Guide. AWS-TR-74-250, (Available at the Library of Congress, Defense Documentation Center (DDC)

Anderson, R. K., et al. 1974: Application of Meteorological Satellite Data in Analysis and Forecasting. Reprint of ESSA Technical Report NESC 51 (including Supplement, Nov. 1971, and Supplement #2, March 1973), U.S. Dept. Commerce, NOAA, NESS, (See p. 5-D-2).

Barkley, R. A., 1968: The Kuroshio-Oyashio Front as a Compound Vortex Street. J. Marine Res., 26, 83-104.

Barkley, R. A., 1972: Jonnston Atoll's wake. J. Marine Res., 30, 201-216.

Beyers, H. R., 1944: General Meteorology. New York: McGraw-Hill Book Co., Inc., P 645.

Cram, R., and K. Hanson, 1974: The Detection by ERTS-1 of Wind-Induced Ocean Surface Features in the Lee of the Antilles Islands. J. Phys. Oceanogr. 4, 594-600.

Emery, K. O., and R. E. Stevenson, 1972: Taiwan--A Ship at Sea. ACTA Oceanographica, Taiwanica, No. 2.

Fons, C., 1966: Wave Forecasting: Spectro-Angular Densities Method No. 5. Cahiers Oceanographiques, 18.

Gelci, R., P. Chavy, and E. Devillaz, 1963: Numerical Treatment of the State of the Sea. Cahiers Oceanographiques 15, 153-160.

Johnson, J. C., 1954: Physical Meteorology, Technology Press of the Mass. Inst. of Tech.; John Wiley and Sons, Inc., N.Y. and Chapman and Hall, Ltd., London, pp. 393.

Lavoie, R. L., 1974: A Numerical Model of Trade Wind Weather on Oahu. Mon. Wea. Rev., 102, 630-637.

Lewis, D., 1974: Wind, Wave, Star, and Bird. National Geographic, 146, 747-793.

McClain, E. P., and A. E. Strong, 1969: On Anomalous Dark Patches in Satellite-Viewed Sunglint Areas. Mon. Wea. Rev., 97, 875-884.

National Aeronautics and Space Administration (NASA), 1968: Earth Photographs from Gemini VI through XII. Scientific and Technical Information Division, pp 327.

Parmanter, F. C., 1969: Picture of the Month--Sunglint. Mon. Wea. Rev., 97, 155-156.

Patzert, W. C., 1969: Eddies in Hawaiian Waters. Hawaii Institute of Geophysics, ONR Contract No. NONR-3748(06), pp 51 and Appendix.

Stevenson, R. E., G. Larson, and C. L. Kober, 1970: Oceanographic Applications of an Earth-Resource Satellite System. Inter-ocean, '70, 2, p. 121-140.

Stevenson, R. E., 1970b: Oceanographic Data Requirements for the Development of an Operational Satellite System, Reprint from: The Proceedings of the Princeton University Conference on Aerospace Methods for Revealing and Evaluating Earth's Resources, held Sept. 25 & 26, 1969 at Princeton, New Jersey. p. 12. 1-12.12.

Strong, A. E., R. J. DeRycke, and H. Stumpf, 1972: Satellite Detection of Upwelling and Cold Water Eddies. Proceedings Eighth Inter Symp. on Remote Sensing of Envir., 1069-1081.

Strong, A. E., R. J. DeRycke, and H. G. Stumpf, 1974: Extensive Areas of Reduced Waves Leeward of the Lesser Antilles. Geo. Res. Letters, 1, 47-49.

White, W. B., 1973: An Oceanic Wake in the Equatorial Undercurrent Downstream from the Galapagos Archipelago, Journal of Physical Oceanography, 3, 156-168.

Wilson, S. W., D. G. Wilson, and J. A. Michael, 1973: Analysis of Swell near the Island of Aruba, J. Geo. Res., 78, 7834-7844.

APPENDIX A
MATHEMATICAL FORMULATION OF THE FRENCH SPECTRO-ANGULAR WAVE MODEL, DSA V

1. Mathematical Formulation

The basic method utilized by the D.S.A. V model to compute the sea state can be illustrated by the following symbolic equation made up of a spectral increase term, a decay term and an advection term:

$$\frac{de}{dt} = F\,[W,\ |\theta - w|,\ T] - \frac{Ae}{T^4}\, m_o - \mathbf{V}_{(T,\theta)}\ \text{Grad}\ e_{(T,\theta)} \qquad (1)$$

where:

m_o is the total sea state developed at a particular time, i.e.:

$$m_o = \int_T \int_\theta e_{(T,\theta)} \qquad (2)$$

and e = the spectro-angular density

$\mathbf{V}_{(T,\theta)}$ = the unit speed of the component, i.e.:

$V_{(T,\theta)} = \frac{gT}{4\pi}$ or the group velocity

W = the surface wind speed in knots

θ = a component azimuth

w = a surface wind azimuth

T = the wave period in seconds

A = the empirical dampening coefficient

F = the spectro-angular increase function

The governing assumptions for the above equation are:

1. Interfering dampening between components is independent of wind direction.
2. The wind direction field can have sixteen values for the azimuth, increasing in a counter-clockwise direction from North.
3. Wind speeds occur within a range of 0 to 85 knots, with speeds less than 5 knots being negligible to sea-state build-up.
4. All components can be grouped into 6 frequency bands, each with a 3-second interval, namely 4, 7, 10, 13, 16 and 19 seconds, respectively.
5. The form of the spectro-angular increase is assumed to be a function of the spectral increase and angular dispersion.

$$F\,[\,W,\ |\theta-w|,\ T\,] = P_{(T,W)} \cdot S(\theta-w) \qquad (3)$$

The spectral increase having the form:

$$P_{(T,W)} \equiv \frac{K}{W^a}\ T^2\ (W - 2T)^3 \qquad (4)$$

and the angular dispersion such that:

$$\int_{-\frac{\pi}{2}}^{-\frac{\pi}{2}} S\ (\theta-w)\ d\ (\theta-w) = 1 \qquad (5)$$

The D.S.A. V model handles dispersion by a series of straight "propagation lines" in the (x,y,t) space. The energy is supplied by subjecting the dx and dy interval to a wind field of velocity, W, and direction w, thus:

$$ds\ dt = \int_0^{2\pi} \int_0^{\infty} \eta\ (T,W,|\theta-w|)\ d\theta dT \qquad (6)$$

where η, the specto-angular growth is

$$\eta = \eta e\ (T, W, |\theta - w|) \tag{7}$$

and

$$\eta e = \frac{de}{dt} + \frac{gT}{4\pi}\frac{de}{dx}\cos\theta + \frac{gT}{4\pi}\frac{de}{dy}\sin\theta \tag{8}$$

$$dt = \frac{de}{d\eta} = \frac{dx}{\frac{gT}{4\pi}\cos\theta} = \frac{dy}{\frac{gT}{4\pi}\sin\theta} \tag{9}$$

6. The spread of the energy dispersion is determined by the period of maximum energy, T. When T is 10 seconds or higher the energy is distributed in 5 directions, for 7 second periods in 3 directions, and for 4 second periods in only 1 direction.

7. Land points cannot receive or transmit energy, while border points can receive energy but not transmit it.

8. Propagation is from grid point to grid point, with the energy being advected at the unit speed:

$$V = \frac{gT}{4\pi} \tag{10}$$

9. The average undulatory for a horizontal element, ds, of the sea-surface is:

$$e = ds \int_0^{2\pi} d\theta \int_0^{\infty} e_{(T,\theta)}\, dT \tag{11}$$

where:

$e_{(T,\theta)}\ dt,\ d\theta\ ds$ = The average undulatory energy between T and T + dT and the direction of propagation between θ and $\theta + d\theta$

$e_{(T,\theta)}$ = The spectro-angular density

From this the average H 1/10 highest waves are computed by:

$$H_{1/10} = 0.16 \sqrt{\int_0^{2\pi} \int_0^{\infty} e_{(T,\theta)}\ d\,T\ d\,\theta} \qquad (12)$$

2. Growth and Decay

Growth in the D.S.A. V model is based on the principal that growth can be represented solely by a function derived from the wind velocity, W, and direction w, as well as the period of the waves formed, T. The spectro-angular density can then be approximated by:

$$e = e\ [\ W,\ |\theta - w|,\ T,\ E\ ] \qquad (13)$$

where E = the sea-state at that time.

The sea-state is considered only with respect to dispersion and thus the energy furnished by the wind fields is independent of E.

Turning to the spectro-angular increase term, Equation (3), it has the following forms for values of W and T:

$$P = \frac{6.76}{W^3} T^2 (W - 2T)^3 \quad ; \text{ if } T < \frac{W}{2} \tag{14}$$

$$P = 0 \quad ; \text{ if } T > \frac{W}{2} \tag{15}$$

The decay in the D.S.A. V model is not an aerodynamic process as such, since the winds do not cause decay directly but through the sea-state components they generate. Decay is also applied through the attentuation of wave trains and at the boundaries of the wave generating areas.

The decay constants used by the model are values of turbulent decay, corresponding to the value of the turbulent viscosity coefficient μ:

$$\mu = 28 \times 10^{-7} m_o \tag{16}$$

where m_o = the total energy density of the developed or developing sea, and has the form:

$$m_o = \int_0^{2k} \int_0^{\infty} e_{(T,\theta)} \, d\,T \, d\,\theta \tag{17}$$

From μ, the decay coefficient for a single component can be found by:

$$\frac{1}{e} \frac{de}{dt} = \frac{6^4 \mu \pi^4}{g^4 \, de \, d\mu} \frac{1}{T^4} = \frac{A}{T^4} m_o \tag{18}$$

where: $e\ d\ T\ d\ \theta$ = the energy density of that component.

$d\ e\ d\ \mu$ = the specific water mass

g = gravity

A = an empirical coefficient

= 18×10^{-9} CGS

Thus leaving:

$$\frac{Ae}{T^4}\ m_o$$

as the decay term, resulting in those waves less than the significant wave height (small m_o) undergoing considerable decay while longer period waves and those above the significant wave height undergo less.

This form of decay has proved to be valid, for the most part, since it has been observed that:

a. The spectral period increases with increasing distance from the generating area.

b. The shorter components undergo strong decay at the borders of the generating area, or, upon crossing another area of strong winds.

c. Longer components, generally undergo weaker decay.

d. Decay decreases as the spectro-angular density, e, decreases.

FIGURES

Figure 1. A DMSP Very High Resolution (VHR) visible depiction on 8 April 1974 at 1853 GMT. Dashed line is the satellite track which crosses the equator at 108.65 W. Subsolar point is located at 7.4 N 102.6 W.

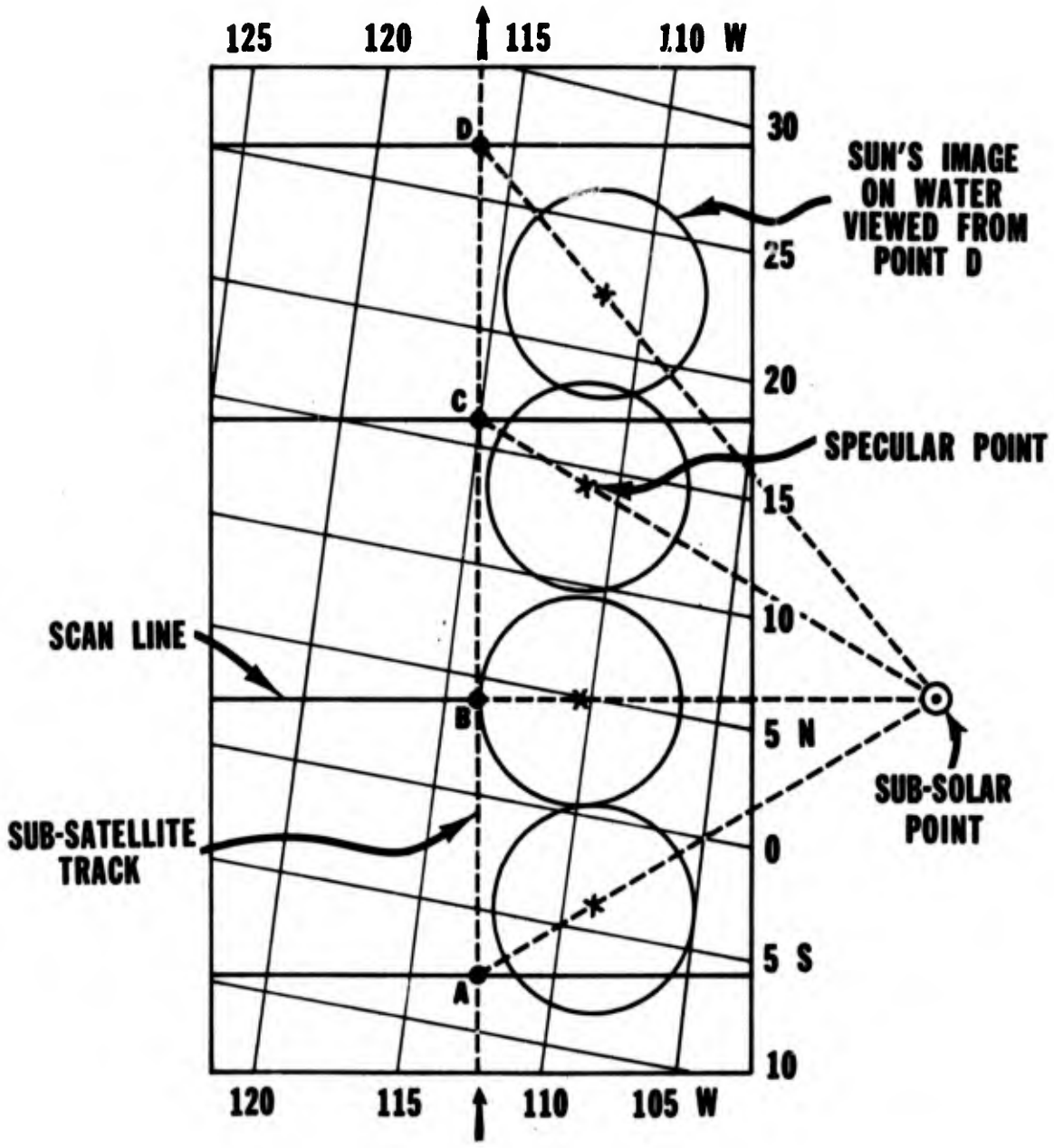

Figure 2. A schematic illustrating sunglint specular point relationships as a function of changing satellite positions, relative to the subsolar point.

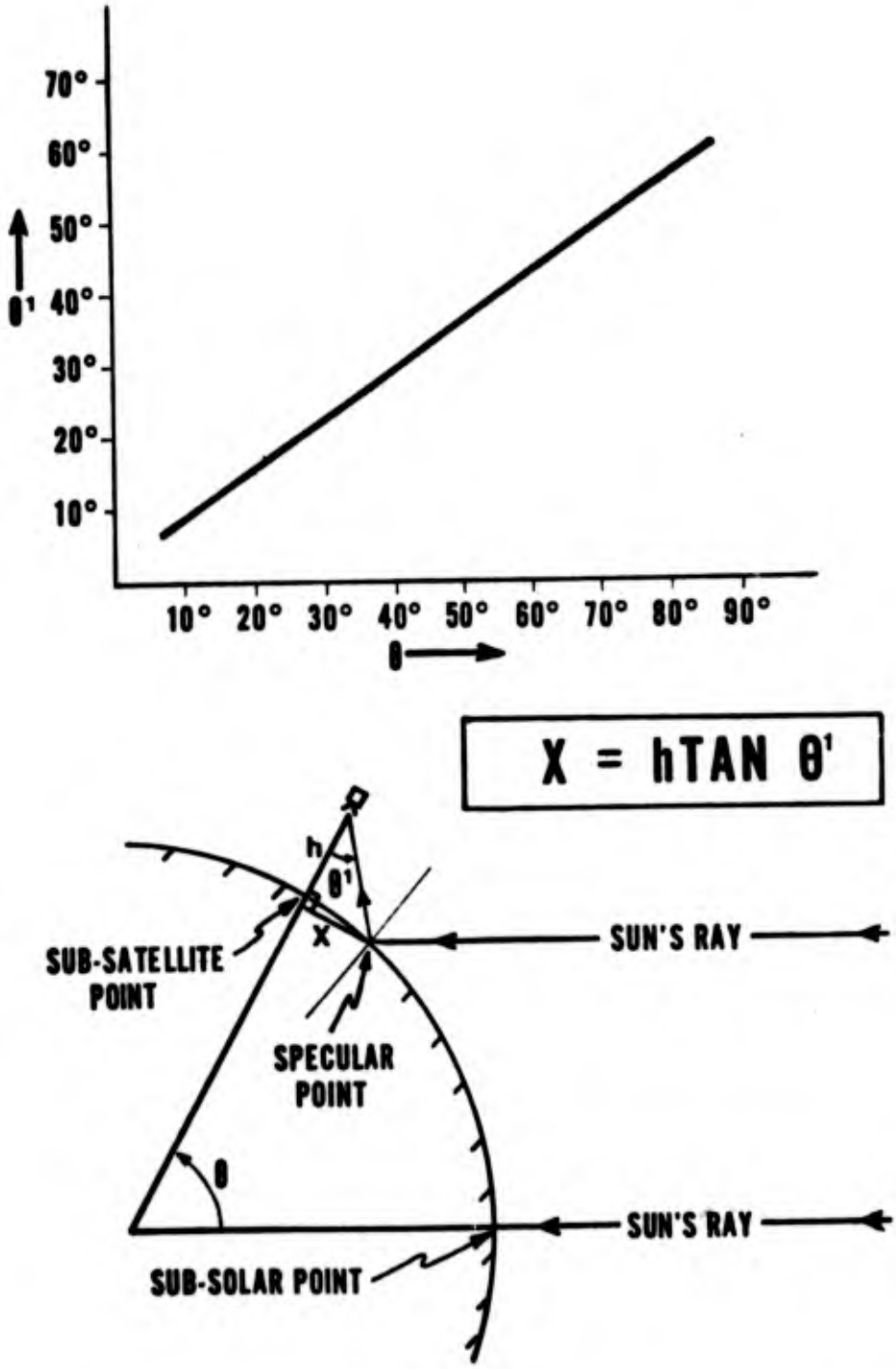

Figure 3. A schematic and nomogram for computing distance to specular point location from the sub-satellite point. The nomogram was developed for a satellite height of 833 km (450 n mi).

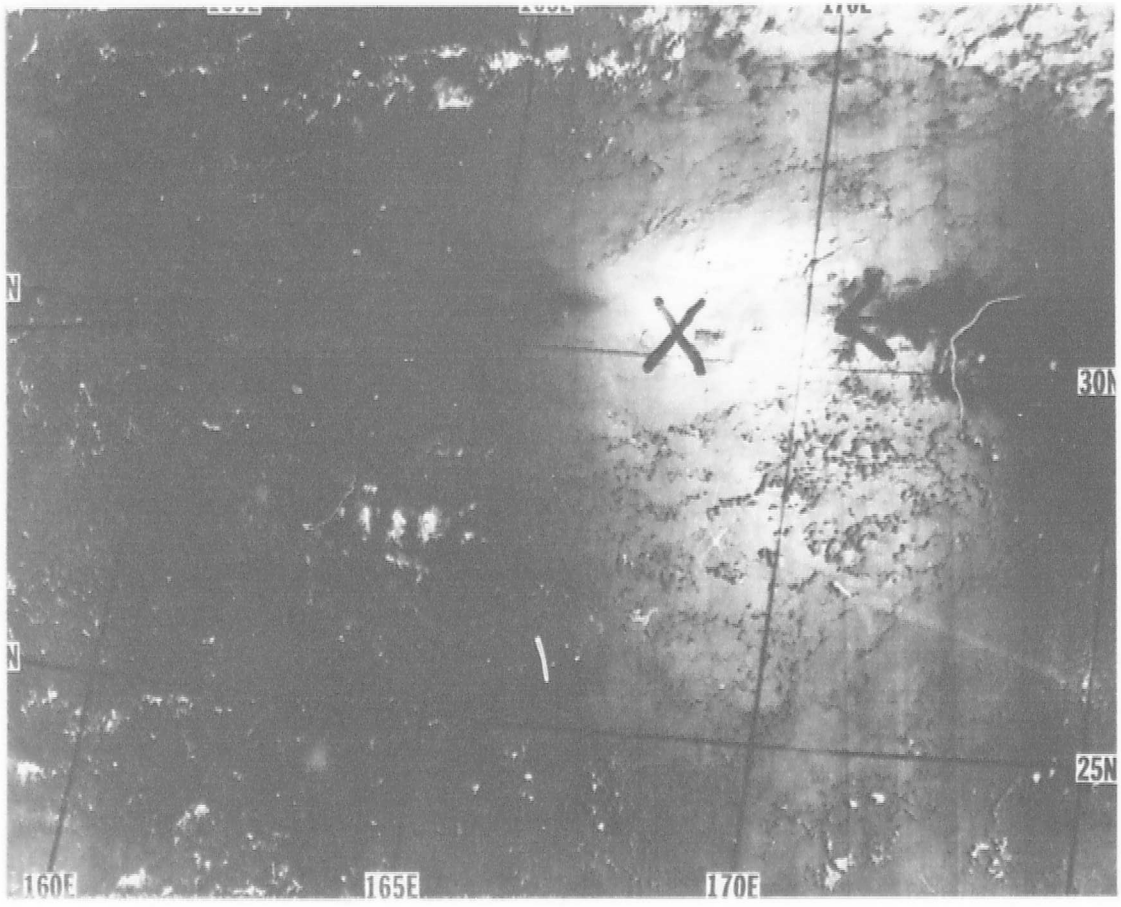

Figure 4. A DMSP VHR visual depiction on 14 July 1974 at 2105 GMT. The dashed line is the sub-satellite track. The circle on the track represents the sub-satellite point. The line through the circle represents a scan line. The specular point location is denoted by an X. The arrow is on the great circle arc connecting the subsolar point, the specular point, and the sub-satellite point. Subsolar point location is 21.6 N 134.8 W.

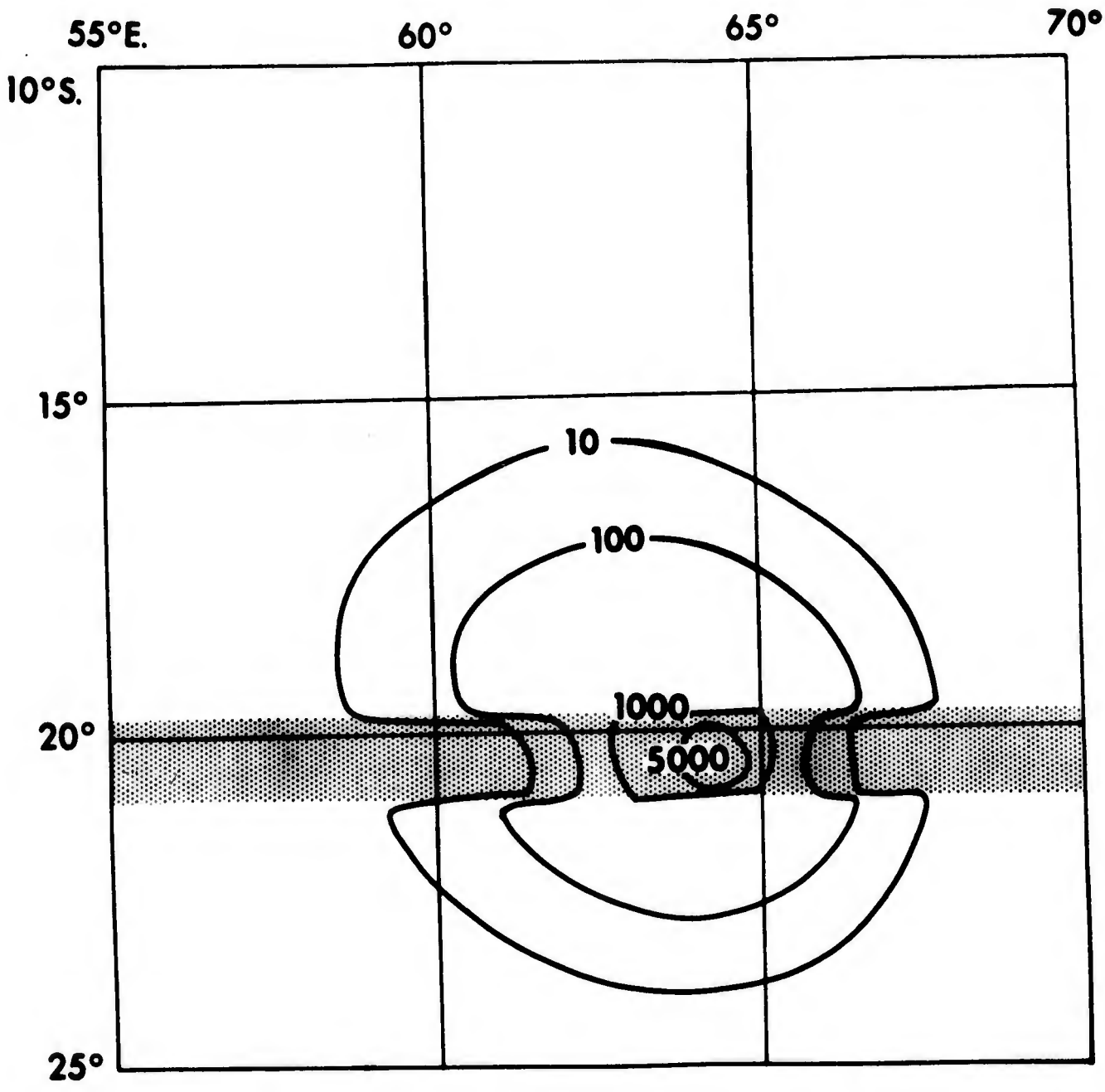

Figure 5. Theoretical sea-surface sunglint for a composite pattern; 5 m sec^{-1} wind background and a calm wind in an east-west swath near specular point (shaded). Isopleths are relative reflected intensity per 10^4 steradian incident flux; sub-satellite point is 21.5 S 65.5 E; subsolar point is 5.8 S 35.6 E, and satellite height is 722 km. (Courtesy McClain and Strong, 1969).

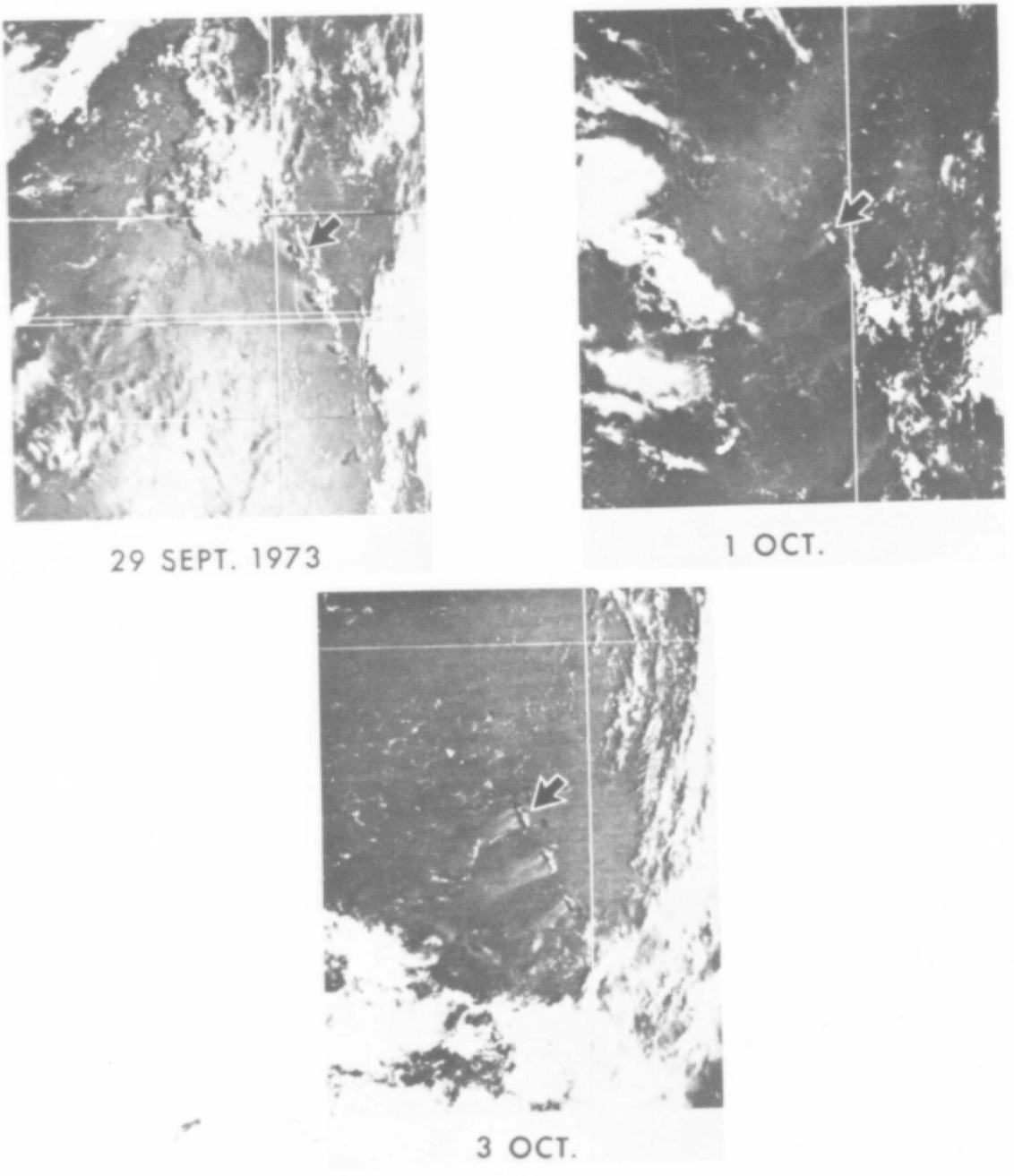

Figure 6. Three Very High Resolution Radiometer (VHRR) images of the Lesser Antilles (white north-south synchronization line is embedded in the image. Arrows point to Guadeloupe Island (Courtesy Strong et al., 1974).

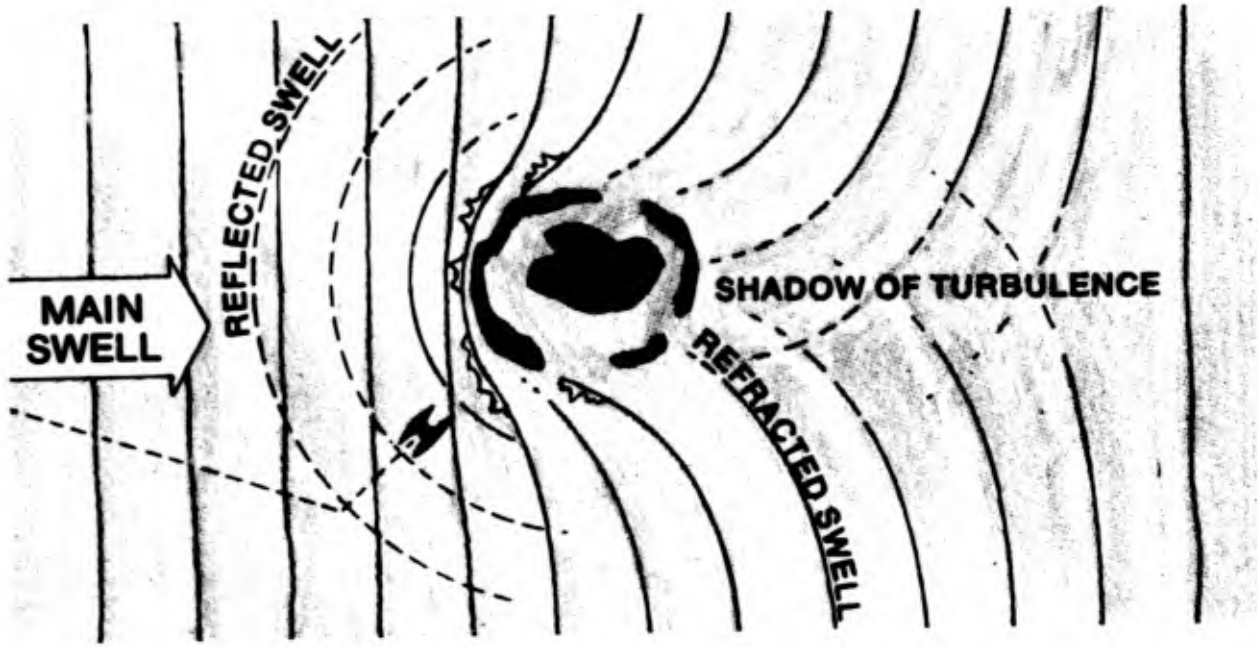

Figure 7. Swell patterns typically noted as refracted around a circular island in the open sea. (Courtesy Lewis, 1974).

Figure 8. A numerically simulated sea height depiction (ft) at hour 39 for a surface wind speed of 7-1/2 m sec^{-1} (2-1/2 m sec^{-1} in lee of island). Sea heights shown are average values for the highest 10% of The swell (H1/10). Average swell height (H) is H 1/10 ÷ 2.03.

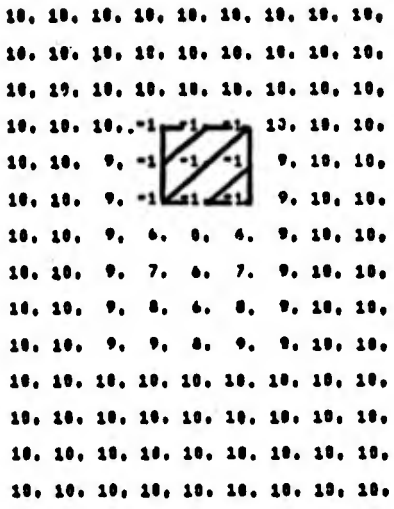

Figure 9. Same as Figure 8 for a surface wind speed of 10 m sec^{-1}.

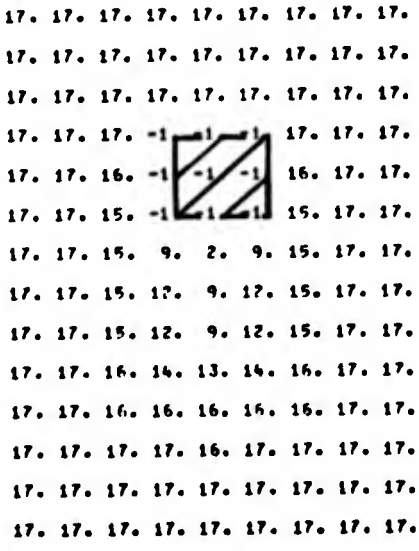

Figure 10. Same as Figure 8 for a surface wind speed of 15 m sec^{-1}.

Figure 11. A numerical simulation of direction of swell around and in the lee of an island, at hour 39, under wind speed conditions of 7-1/2 m sec^{-1}.

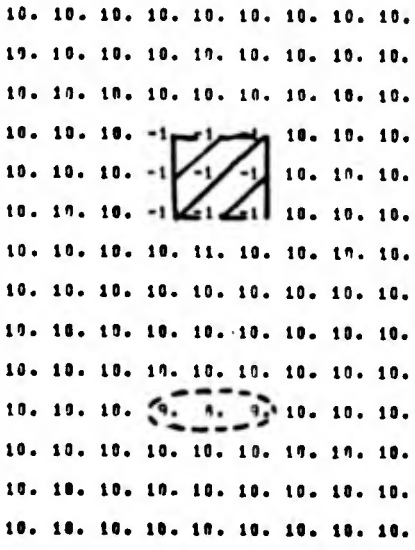

Figure 12. A numerical simulation of swell period (in seconds), around and in the lee of an island, at hour 9, under wind speed conditions of 15 m sec^{-1}.

Figure 13. Same as Figure 12, except conditions are for hour 39 with wind speeds of 15 m sec^{-1}.

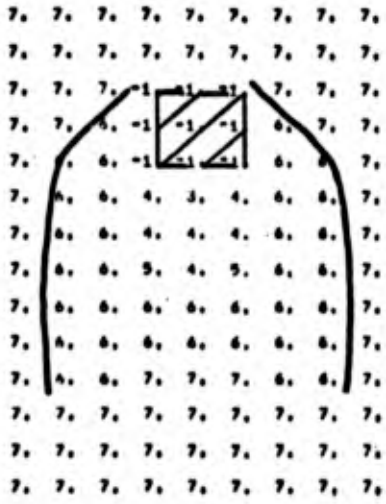

Figure 14. A numerical simulation of swell height at hour 15 under wind speed conditions of 7-1/2 m sec^{-1}. Sea heights shown are average values for the highest 10% of the swell (H 1/10). Average swell height (H) is H 1/10 - 2.03.

Figure 15. A numerical simulation of swell direction at hour 15 under wind speed conditions of 7-1/2 m sec^{-1}.

N	0	*	0	0	0	0	0	0
NNE	0	*	0	0	0	0	0	0
NE	1	*	0	1	0	0	0	0
ENE	2	*	0	1	0	0	0	0
E	6	*	1	5	0	0	0	0
ESE	6	*	1	5	0	0	0	0
SE	3	*	0	2	0	0	0	0
SSE	0	*	0	0	0	0	0	0
S	0	*	0	0	0	0	0	0
SSW	0	*	0	0	0	0	0	0
SW	0	*	0	0	0	0	0	0
WSW	0	*	0	0	0	0	0	0
W	0	*	0	0	0	0	0	0
WNW	0	*	0	0	0	0	0	0
NW	0	*	0	0	0	0	0	0
NNW	0	*	0	0	0	0	0	0
TOTAL	20		3	16	0	0	0	0
	PERIODS		4	7	10	13	16	19

Figure 16. Breakdown of Spectral Energy Components, joules cm^{-2}, for Southern Point of Anomalous Wave Direction, 292°.

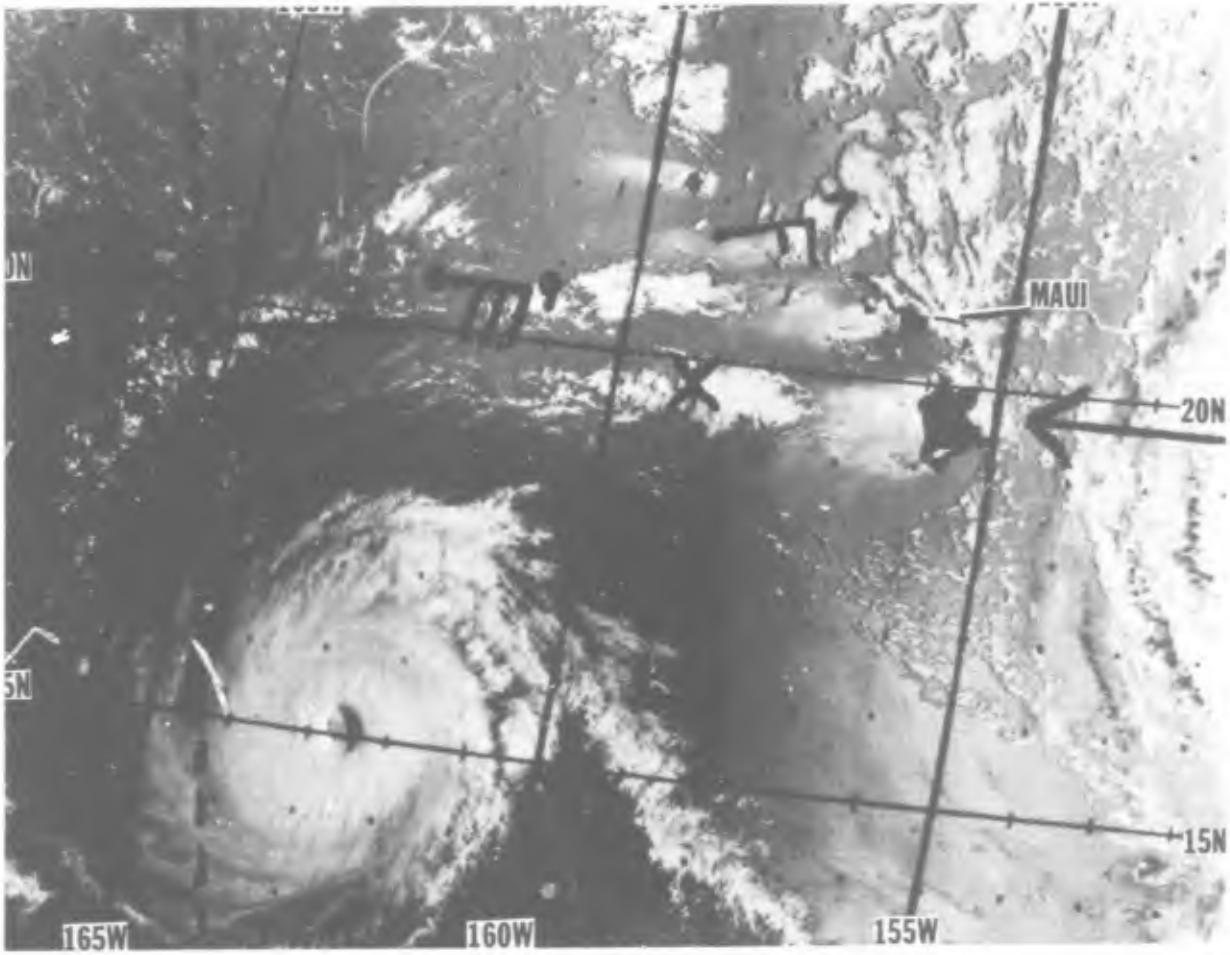

Figure 17. A DMSP VHR visual depiction on 17 August 1972 at 1917 GMT. The dashed line is the sub-satellite track. The circle on the track represents the sub-satellite point. The line through the circle represents a scan line. The specular point location is denoted by an X. The arrow is on the great circle arc connecting the subsolar point, and the sub-satellite point. Subsolar point location is 13.2 N/108.3 W. Wind reports are in knots (1 barb = 10 kt). Hurricane Celeste (intensity 85 kt) appears SW of the island chain.

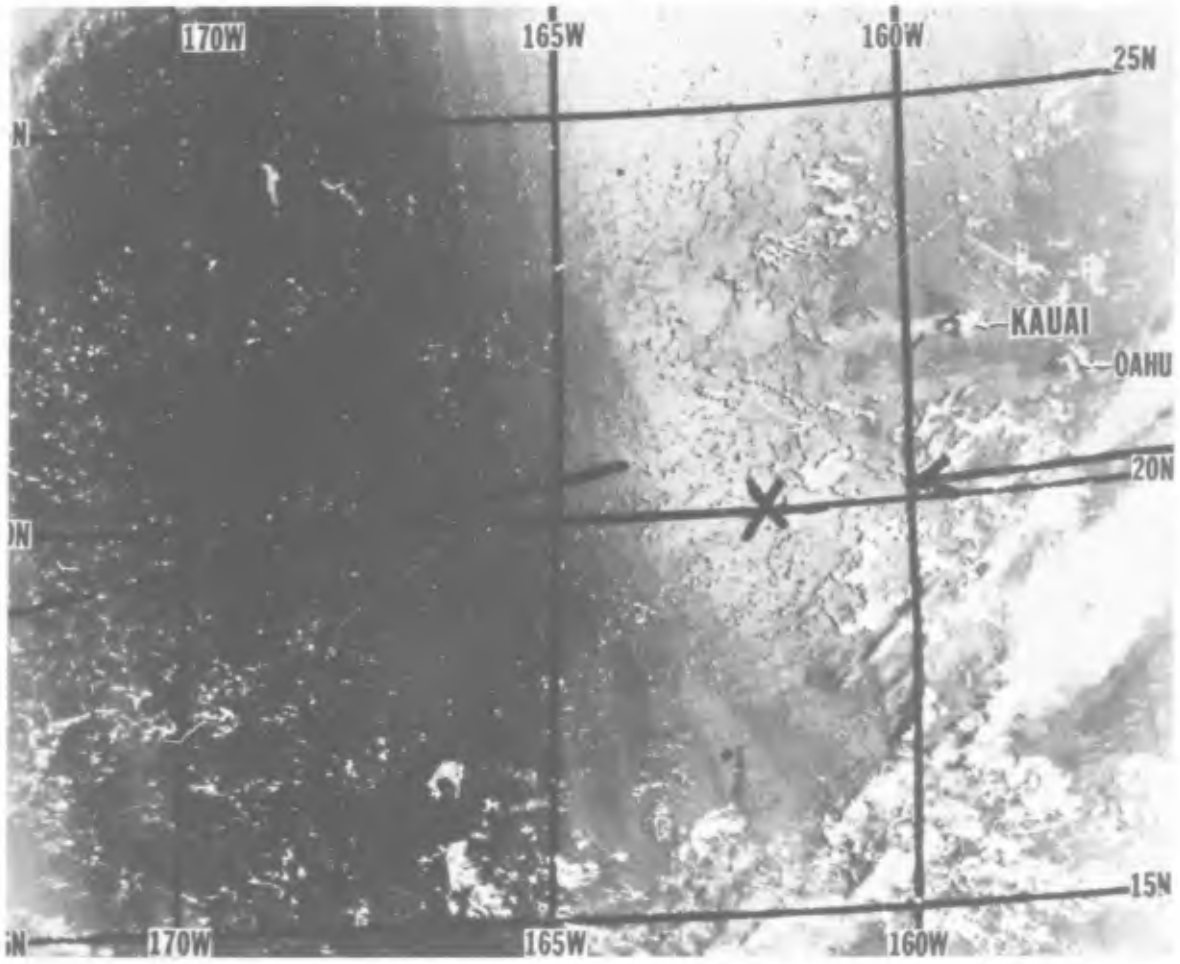

Figure 18. A DMSP VHR visual depiction on 30 June 1974 at 1935 GMT. The dashed line is the sub-satellite track. The circle on the track represents the sub-satellite point. The line through the circle represents a scan line. The specular point location is denoted by an X. The arrow is on the great circle arc connecting the subsolar point, the specular point, and the sub-satellite point. Subsolar point location is 23.1 N/112.9 W.

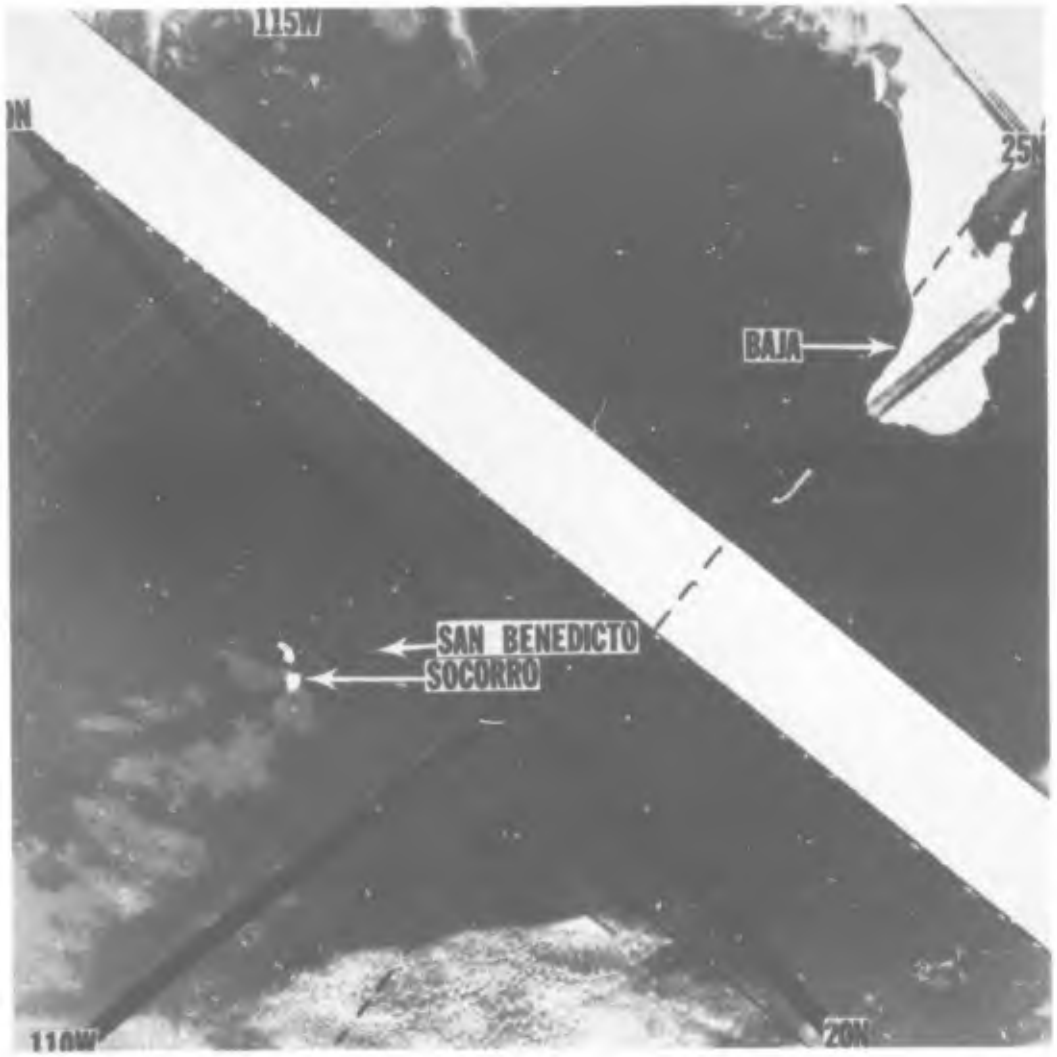

Figure 19. A DMSP VHR visual depiction on 5 November 1974 at 1928 GMT. The dashed line is the sub-satellite track. The circle on the track represents the sub-satellite point. The line through the circle represents a scan line. The specular point location is off the picture 424 km to the SSW. The arrow is on the great circle arc connecting the subsolar point, the specular point, and the sub-satellite point. Subsolar point location is 15.75/116 W.

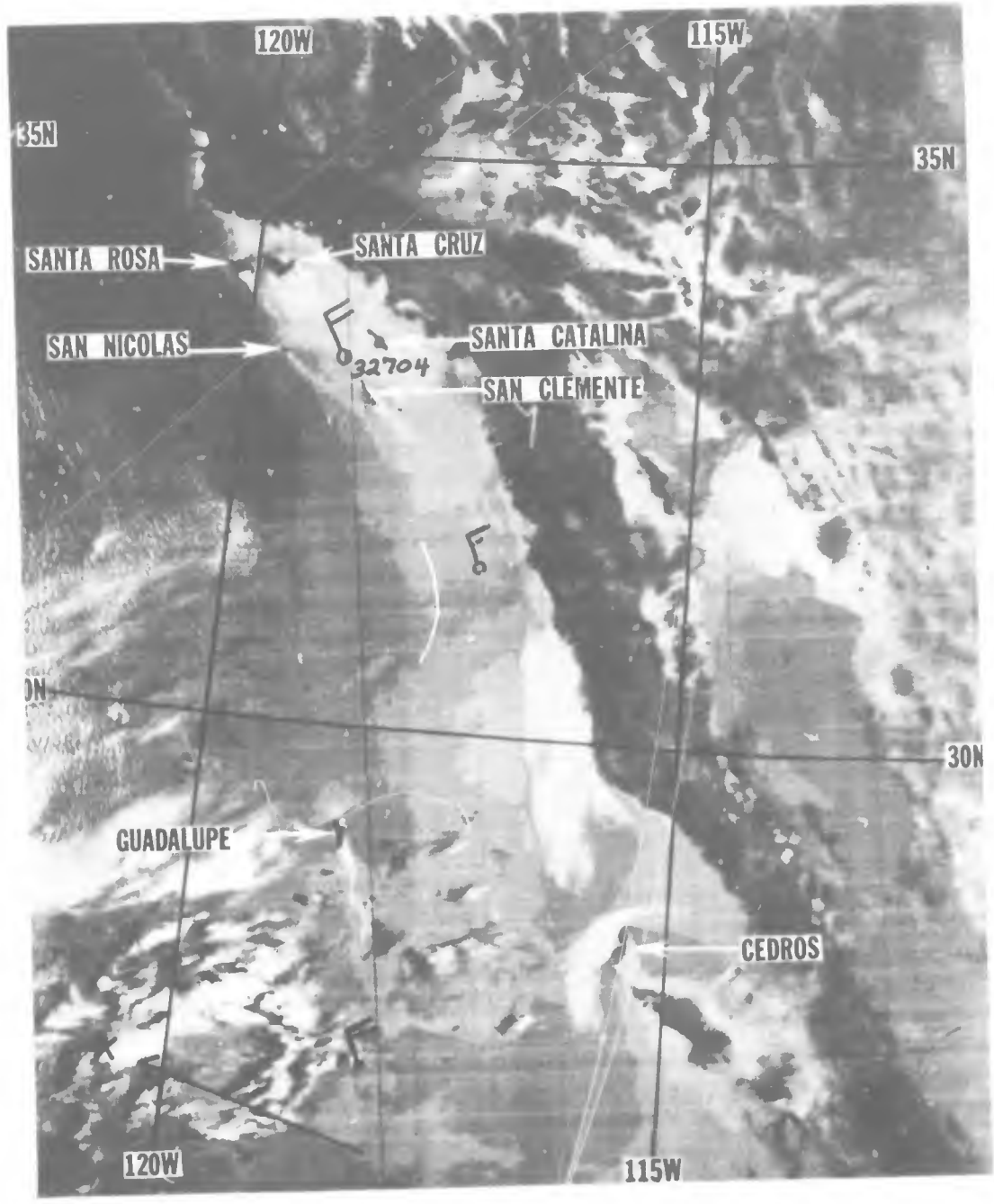

Figure 20. A DMSP VHR visual depiction on 21 May 1974 at 1632 GMT. The sub-satellite track and the sub-satellite point are off of picture. The specular point location is denoted by an X. The arrow is on the great circle arc connecting the subsolar point, the specular point, and the sub-satellite point. Subsolar point location is 20.2 N/68.5W. The sea-state group, 32704, indicates swell from 320° with a period of 7 seconds, and a height of about 2 m.

Figure 21. A DMSP VHR visual depiction on 8 May 1973 at 1920 GMT.

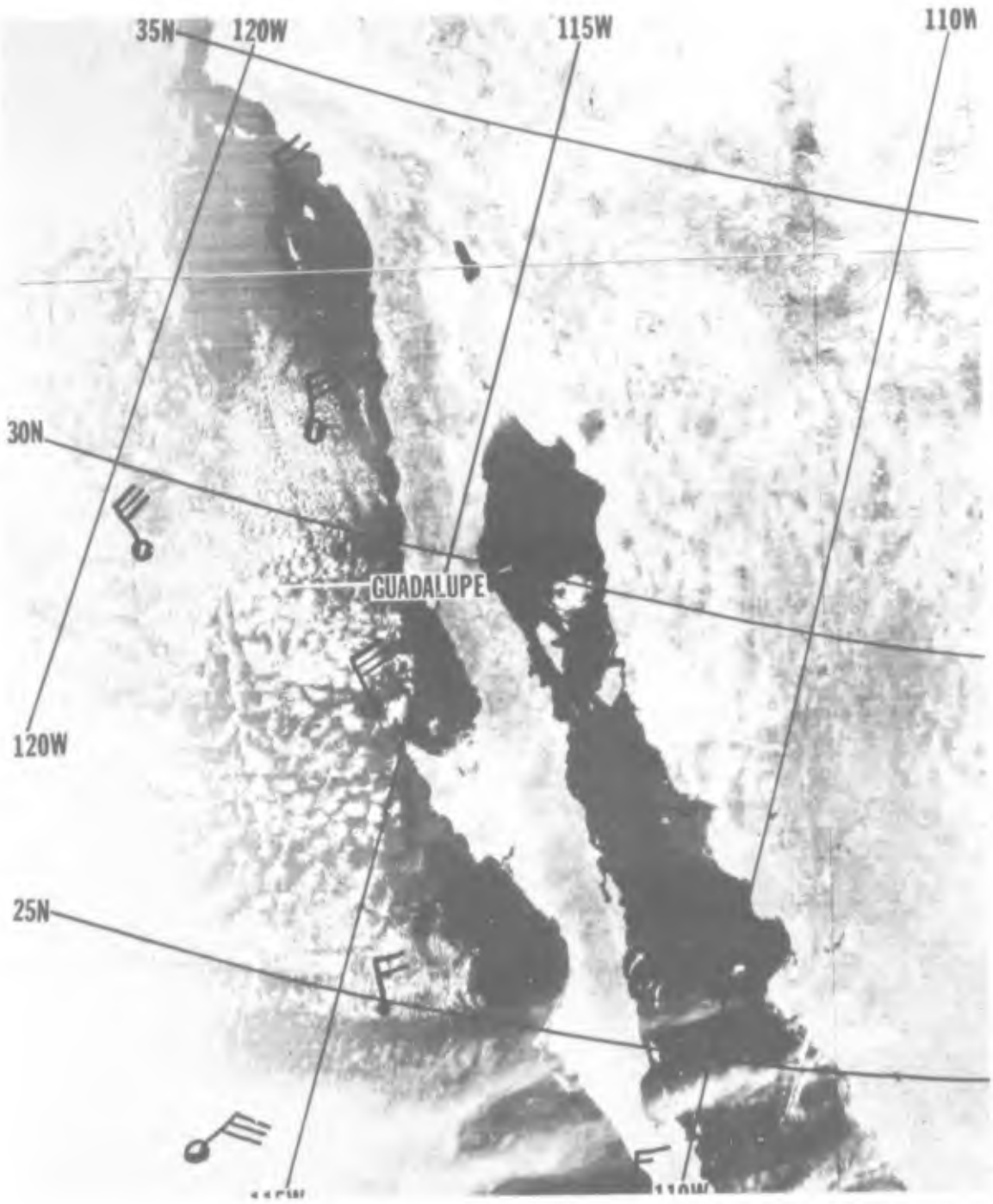

Figure 22. A DMSP VHR visual depiction on 10 April 1974 at 1816 GMT. Wind reports are as in Figure 17.

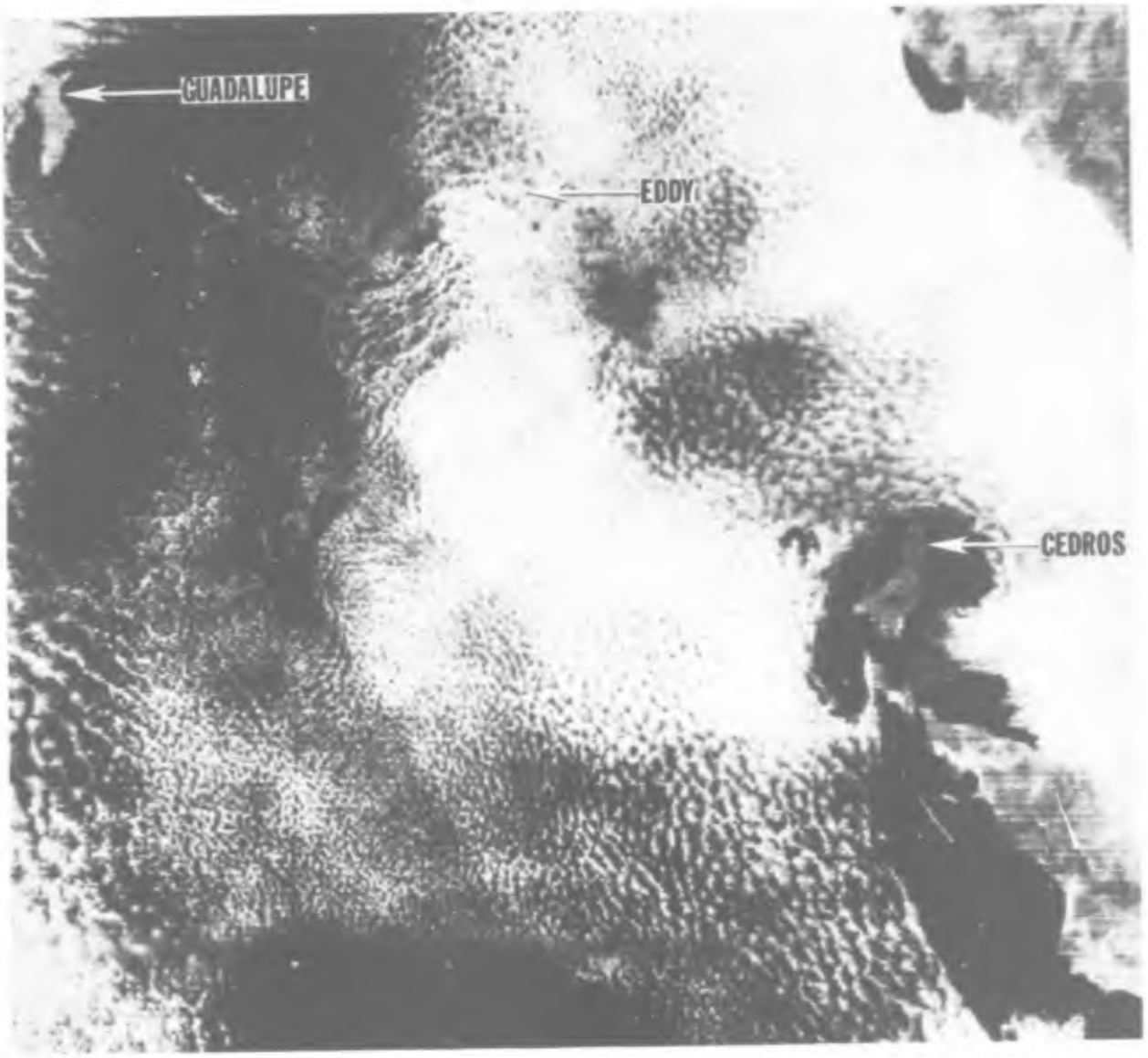

Figure 23. A DMSP VHR visual depiction on 8 April 1974 at 1853 GMT.

Figure 24. A DMSP VHR visual depiction on 22 May 1974 at 1613 GMT.

Figure 25. An ERTS view on 22 May 1974 at 1806 GMT. Depiction is from Channel 5, .6-.7 micrometer spectral interval.

Figure 26. A DMSP VHR visual depiction on 22 May 1974 at 1850 GMT.

Figure 27. A DMSP VHR visual depiction on 11 April 1974 at 1758 GMT.

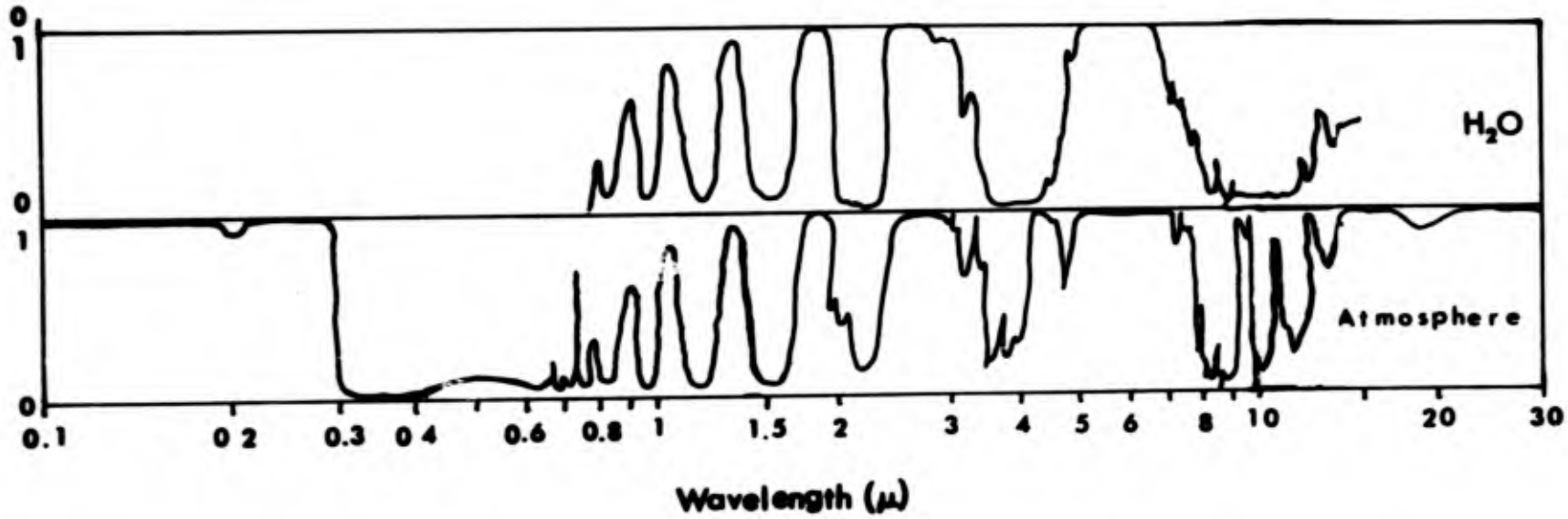

Figure 28. Absorptivity curves. Entire atmospheric effect is shown in the bottom half of figure and that for water vapor in the upper half.

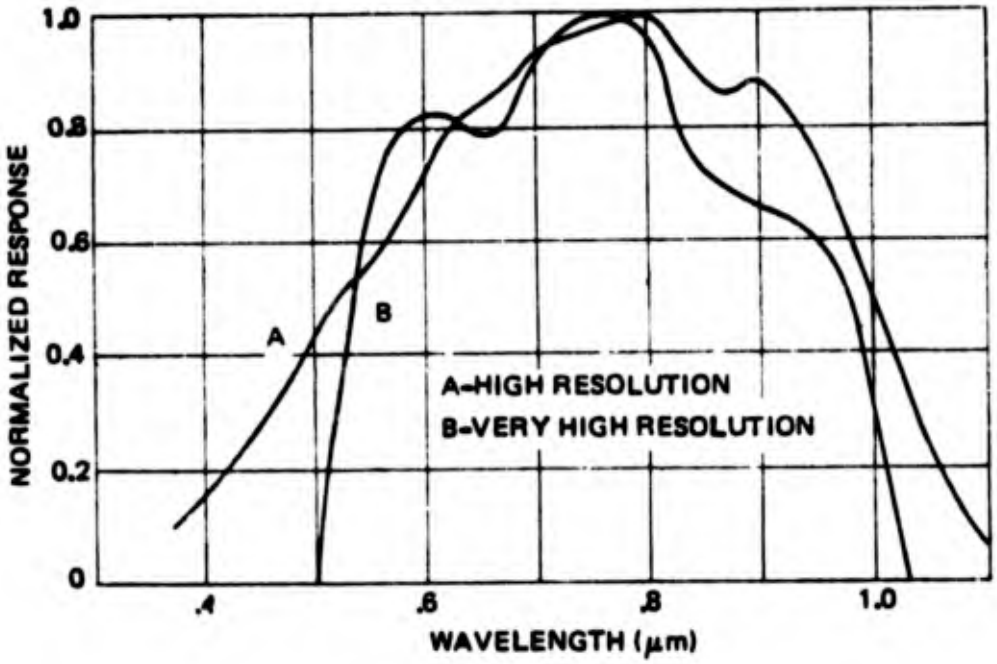

Figure 29. DMSP visual channel spectral response.

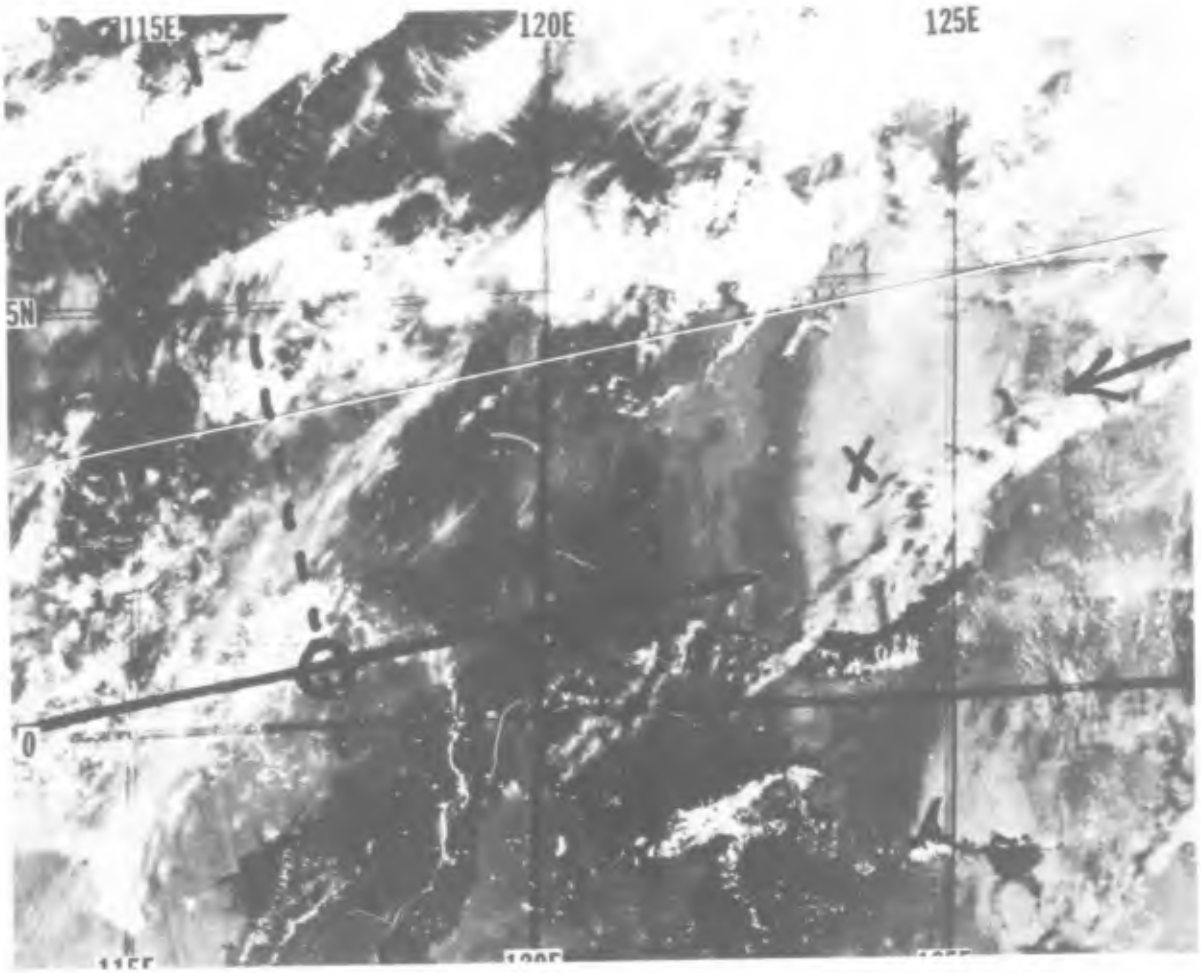

Figure 30. A DMSP VHR visual depiction on 14 August 1974 at 0047 GMT. The dashed line is the sub-satellite track. The circle on the track represents the sub-satellite point. The line through the circle represents a scan line. The specular point location is denoted by an X. The arrow is on the great circle arc connecting the subsolar point, the specular point, and the sub-satellite point. Subsolar point location is 14.6 N/169.4 E.